

Comparison of the CME-shock Acceleration of Three Widespread SEP Events during Solar Cycle 24

H. Xie,^{1,2} P. Mäkelä,^{1,2} O. C. St. Cyr,² and N. Gopalswamy²

¹Department of Physics, The Catholic University of America, Washington DC, USA.

²Code 670, NASA/Goddard Space Flight Center, Greenbelt, Maryland, USA

Copyright 2017 by the American Geophysical Union.

0148-0227/17/\$9.00

Abstract.

We studied three solar energetic particle (SEP) events observed on August 14, 2010, November 03, 2011, and March 05, 2013 by STEREO A, B and near-Earth (L1) spacecraft with a longitudinal distribution of particles > 90 degree. Using a forward-modeling method combined with extreme ultraviolet and white-light images we determined the angular extent of the shock, the time and location (cobpoint) of the shock intersection with the magnetic field line connecting to each spacecraft, and compute the shock speed at the cobpoint of each spacecraft. We then examine whether the observations of SEPs at each spacecraft were accelerated and injected by the spatially extended shocks or whether another mechanism such as cross-field transport is required for an alternative explanation. Our analyses results indicate that the SEPs observed at the three spacecraft on November 03, STB and L1 on August 14, and the March 05 SEP event at STA can be explained by the direct shock acceleration. This is consistent with the observed significant anisotropies, short time delays between particle release times and magnetic connection times, and sharp rises in the SEP time profiles. Cross-field diffusion is the likely cause for the August 14 SEP event observed by STA and the March 05 SEPs observed by STB and L1 spacecraft, as particle observations featured weak electron anisotropies and slow rising intensity profiles. Otherwise, the wide longitudinal spread of these SEP increases would require an existence of a circumsolar shock, which may not be a correct assumption in the corona and heliosphere.

1. Introduction

Multi-spacecraft observations from the Solar Terrestrial Relations Observatory (STEREO) A and B (Kaiser et al., 2008) and from near-Earth spacecraft at the Lagrange point (L1) has provided us a great opportunity to study the longitudinal extent of solar energetic particle (SEP) events. *Richardson et al.* [2014] compiled a catalog of more than 200 individual > 25 MeV solar proton events occurring during solar cycle 24. They found that there is a subset of 25 events observed by all three spacecraft (the two STEREOs and L1 spacecraft). These large SEP events are usually associated with fast and wide CMEs that propagated outward driving coronal shocks expanding to large distances encompassing and wrapping around the Sun.

It was generally believed that an expanding coronal shock can cause the longitudinal spread of SEP events of at least 100 degrees [*Kallenrode et al.*, 1993; *Cane and Erickson*, 2003]. However, *Cliver et al.* [1995] used observations from IMP-8 and Helios 1 and 2 and found a CME driven-shock that resulted in an SEP event with a spread of $\sim 150^\circ$ in longitude, implying that a coronal shock may extend up to $\sim 300^\circ$. *Cliver et al.* [1995] studied an extended farside (\sim W180) CME event that was associated with 400 MeV protons at L1 and proposed that such a wide spread in longitude was caused by expanding CME shocks that span up to 300–360 degrees, i.e., essentially circumsolar shocks. Recent STEREO and the Solar and Heliospheric Observatory (SOHO) [*Domingo et al.*, 1995] observations have provided more evidence of such wide SEP events [e.g. *Rouillard et al.*, 2012; *Wiedenbeck et al.*, 2013; *Prise et al.*, 2014; *Richardson et al.*, 2014]. Using ^3He ion data from STEREO and the Advanced Composition Explorer (ACE) spacecraft, *Wieden-*

beck et al. [2013] found that energetic ions associated with an impulsive flare on 2010 February 7 could be observed over a wide range of $\sim 136^\circ$ in longitude. *Rouillard et al.* [2012] and *Prise et al.* [2014] conducted case studies for two multi-spacecraft SEP events caused by fast and wide CMEs on 2011 March 21 and 2011 November 03. They found that the particle onset delays were consistent with the time needed for the coronal shock to expand to the longitude of the magnetic foot point connected to the observing spacecraft. On the other hand, *Lario et al.* [2014] and *Lario et al.* [2016] studied two widespread SEP events observed on 2014 April 11 and 2014 February 25 and found that not all of the associated EUV waves reached the footpoint of the field lines connecting each observer with the Sun. They suggested that the expansion of the CME-driven shock at high altitudes above the solar surface, instead of EUV waves, determined the SEP injection and SEP intensity-time profiles at different longitudes. In addition, *Miteva et al.* [2014] studied a greater number of SOHO Extreme ultraviolet Imaging Telescope (EIT) waves and found that the release times of near-relativistic electrons were too early compared to the timing of the intersection of the EIT waves and the observer's magnetic footpoint in many events. They also indicated that the observed weak anisotropy of the electrons posed a problem for the idea that the SEPs were accelerated by the EIT wave, suggesting a combination of a spatially extended shock acceleration and cross-field transport as an alternative explanation.

In this paper, we use forward modeling with a three-dimensional (3D) flux rope (FR) plus oblate spheroid shock model to analyze three SEP events. The three SEP events occurred on 2010 August 14, 2011 November 03, and 2013 March 05, which are selected based on the criterion that a significant electron anisotropy was observed by only one

spacecraft, or two spacecraft or all three spacecraft, respectively [Dresing *et al.*, 2014]. All three SEP events show widespread longitudinal distribution of particles ($> 90^\circ$) but with different onset delays, intensity profiles, and electron anisotropies. By fitting the FR plus shock model to white-light and extreme-ultraviolet (EUV) images from STEREO, SOHO and SDO, we are able to best determine the 3D shape of the CME shock. The forward-modeling technique constrained with multi-spacecraft observations allows us to determine the location where the shock front intersects the magnetic field line connecting to the observing spacecraft, also known as cobpoint (Connecting with the OBserver point), and compute the shock speed and expansion speed at the cobpoints. We examine the angular extent of the CME shock and its height and speed at the cobpoint of each spacecraft in order to investigate whether the observed widespread SEP events can be explained by the expansion of the CME-driven shock or whether an alternative explanation such as cross-field transport is needed for the observed SEPs.

The paper is organized as follows. In section 2 we give an overview of associated solar observations, observations of electron and proton fluxes and how we determine SEP onset and solar particle release (SPR) times. In section 3 we introduce the forward modeling method and present the fitting results of the CME shock. In section 4 we provide the formalism to determine the shock height and speed at cobpoint of each observing spacecraft. Finally, section 5 presents summary and discussion.

2. Observations

2.1. Solar Observations

In Table 1, we list the event number (column 1) and date (column 2) for the three SEPs, and associated flare onset time and flare location (columns 3–4), CME sky-plane and space

speeds (columns 5–6), type II and type III radio burst onset times (columns 6–7), and connection angle (CA) for STEREO-A (STA), STEREO-B (STB), and near-Earth (L1) spacecraft (columns 8–10), where CA is defined as the longitudinal angular distance between the flare location and the estimated magnetic footpoint of each spacecraft. A positive CA denotes a SEP source to the west of the spacecraft magnetic footpoint while negative value denotes a source to the east. The CME plane-of-sky speeds are extracted from the CDAW halo CME list (http://cdaw.gsfc.nasa.gov/CME_list/halo/halo.html), and the metric type II and type III burst data are from (http://cdaw.gsfc.nasa.gov/CME_list/NOAA/org_events_text/) and (<http://cdaw.gsfc.nasa.gov/images/wind/waves/>).

Figure 1 shows longitudinal configurations of spacecraft, their magnetic footpoints and SEP solar sources for the three events. The black arrow marks the longitude of the SEP source, which is identified as the location of the associated flare in movies of EUV images by the Atmospheric Imaging Assembly [AIA; *Lemen et al.*, 2012] on the *Solar Dynamics Observatory* (SDO) spacecraft and by the EUV Imager [EUVI; *Wuelser et al.*, 2004; *Howard et al.*, 2008] on the STEREO spacecraft. The red, blue, and green spots mark the locations of STA, STB, and near-Earth (L1) spacecraft (i.e., SOHO, ACE and Wind). The colored spirals are the nominal Parker field lines connecting the spacecraft to the Sun, which are computed using in-situ solar wind speeds measured at each spacecraft at the onset of the SEP event, as summarized in Table 2.

The 2010 August 14 SEP event was associated with a C4.4 X-ray flare at N17W52 at AR11099. The observed metric type II and type III radio burst onsets occurred at 09:52 UT and 09:56 UT, respectively. It is a well-connected event for both L1 spacecraft (CA = 4°) and STB (CA = 48°). Both the Three-dimensional Plasma and Energetic Particles

instrument [3DP; *Lin et al.*, 1995] on the Wind spacecraft and the Solar Electron Proton Telescope [SEPT; *Müller-Mellin et al.*, 2008] on STB observed a significant anisotropy with A values > 0.6 [*Dresing et al.*, 2014], where they defined the anisotropy A as

$$A = \frac{3 \int_{-1}^{+1} I(\mu) \cdot \mu \cdot d\mu}{\int_{-1}^{+1} I(\mu) \cdot d\mu} \quad (1)$$

where $I(\mu)$ is the intensity at a given pitch-angle direction and μ is the pitch angle cosine.

The 2011 November 03 SEP event occurred behind the east-limb as viewed from the Large Angle and Spectrometric Coronagraph (LASCO) onboard SOHO [*Brueckner et al.*, 1995]. The associated flare location was N09E154 (as seen from Earth). Since the longitude of STA was \sim W105 and that of STB was \sim E102 away from Earth, the source location was \sim W101 and \sim E52 in the STA and STB view respectively. The SEP event is well-connected to STA (CA = 11°) but poorly-connected to both the STB and L1 spacecraft with CA $> 130^\circ$. All three spacecraft (WIND, STA and STB) observed a high anisotropy with A values > 1.6 [*Gómez-Herrero et al.*, 2015].

The 2013 March 05 CME occurred also behind the east-limb as seen from SOHO/LASCO and its flare location of N10E144 was similar to the 2011 November 03 SEP event. However, since STA had drifted further away from Earth to \sim W131 (STB \sim E140), the source location is \sim W85 and \sim E04 in the STA and STB view respectively. The CA of the SEP event was 14° for STA, 94° for STB, and 152° for the L1 spacecraft. Again the SEP is well-connected to STA but poorly-connected to both STB and L1 spacecraft. Only STA/SEPT observed a significant anisotropy with A values > 0.6 [*Dresing et al.*, 2014].

2.2. SEP Observations: Solar Particle Release Time

Time-shifting analysis (TSA) and velocity dispersion analysis (VDA) are two commonly used methods to infer the solar particle release (SPR) time from the SEP in-situ observations at 1 AU [e.g. *Krucker et al.*, 1999; *Tylka et al.*, 2003; *Malandraki et al.*, 2012; *Vainio et al.*, 2013]. The TSA computes the SPR time by shifting the onset time by the particle travel time along the nominal Parker spiral field line: $t_{SPR} = t_{onset} - l/v$, where l is the nominal path length from the Sun to the spacecraft and v is the particle speed. The result of TSA represents the latest possible release of SEPs. It is a good approximation if the SEPs travel nearly scatter free at nearly zero pitch angle along the magnetic field line. In this study we used the VDA method to estimate the release time of SEPs.

The VDA infers the particle release time and the travel path length based on the assumption that particles at all energies are released simultaneously and travel the same path length. The particle arrival time at 1 AU is given by:

$$t_{onset}(E) = t_0 + 8.33 \frac{\text{min}}{\text{AU}} L(E) \beta^{-1}(E) \quad (2)$$

where $t_{onset}(E)$ is the onset time in minutes observed at the energy E , t_0 is the release time in minutes at the Sun, L is the path length travelled by the particle in units of AU and $\beta^{-1}(E) = c/v(E)$ is the inverse speed of the particles. If energetic particles travel the same path length and are released at the same time, then a linear dispersion relation can be obtained by plotting onset times of the particle increase versus β^{-1} in each energy channel. The slope and the intersection with the time axis of the linear fit yield the path length and the particle release time at the Sun, respectively.

The SEP onset times in all energy channels included in the VDA are estimated using the Fixed-Onset-Level method. The Fixed-Onset-Level method identifies the onset time as the time when the intensity rises to a certain percentage of the peak value, say, 1.0% of the maximum event intensity. This onset level is also required to be at least 3δ deviations above the background levels in all energy channels [see details in *Xie et al.*, 2016]. The selected onset levels are dependent on both the details of the pre-event conditions and the spacecraft instruments, because they cause variation of the background levels in different SEP channels. The usage of the Fix-Onset-Level onset times allows us to avoid the background effects [e.g. *Lintunen and Vainio*, 2004; *Laitinen et al.*, 2010] introduced by varying background levels in different VDA energy channels. Although the obtained VDA path lengths increase as the onset levels increase, *Xie et al.* [2016] showed that the VDA release times remain roughly the same within an uncertainty of ~ 10 min for different onset levels.

Figure 2 first row shows the electron fluxes for the 2010 August 14 event: (a) 5-min average electron intensity in the 50–115 keV energy channels from STB/SEPT, (b) 5-min average electron intensity in the 27–180 keV energy channels from Wind/3DP and (c) 30-min average electron intensity in the 50–95 keV energy channels from STA/SEPT pointing towards the solar direction. Note that in the figure, for weak SEPs observed at STA/SEPT, we used longer time averages (30 min) to improve the statistics at the expense of losing time resolution. Similar longer time averages were used for STA/LET proton data on 2010 August 14, WIND/3DP electron data, STB/HET proton data and SOHO/ERNE proton data on 2013 March 5. The red vertical dashed line in the plot marks the onset time of the associated type III radio burst. As expected, the particle event was the most

intense with the earliest onset at the best-connected Wind spacecraft. The STB/SEPT intensity was around one order of magnitude lower than the Wind/3DP intensity, and the STA/SEPT intensity was around two orders of magnitude lower with a slow rise, making the onset times ill-defined due to a low signal-to-noise ratio. In order to improve the counting statistics, longer time (30-min) periods were used in calculating the average STA/SEPT intensities. Figure 2 second row shows: (d) 10-min average proton intensity in the 4.25–9 MeV energy channels from the Low Energy Telescope [LET; *Mewaldt et al.*, 2008] on STB, (e) 5-min average proton intensity in the 15.4–72 MeV energy channels from the Energetic and Relativistic Nuclei and Electron instrument [ERNE; *Torsti et al.*, 1995] on SOHO, and (f) 30-min average proton intensity in the 4.25–9 MeV energy channels from STA/LET. The third row of Figure 2 shows the VDA results for the three spacecraft where onset levels of 1%, 2% and 60% were used for Wind/3DP, STB and STA/SEPT electron data, and 1%, 1.2% and 5.5% for SOHO/ERNE, STB and STA/LET proton data, respectively. No high-energy contamination was found in this event due to a relatively weak SEP intensity in the higher energy channels.

Figure 3 first row shows the electron fluxes for the 2011 November 03 event: (a) 10-min average electron intensity in the 50–240 keV energy channels from STB/SEPT, (b) 10-min average electron intensity in the 39–513 keV energy channels from Wind/3DP and (c) 5-min average electron intensity in the 50–240 keV energy channels from STA/SEPT pointing towards the solar direction. The red vertical dashed line in the plot marks the onset time of the associated type III radio burst. The particle event was the most intense with an abrupt increase at the best-connected STA. The STB/SEPT intensity was around one order of magnitude lower than the STA/SEPT intensity, and the intensity had a rela-

tively sharp increase. WIND/3DP measured a similar intensity as STB/SEPT but with a slower rise. Figure 3 second row shows: (d) 10-min average proton intensity in the 14.4–50 MeV energy channels from the High Energy Telescope [HET; *von Rosenvinge et al.*, 2008] on STB, (e) 10-min average proton intensity in the 25.3–50.4 MeV energy channels from The Energetic Particles: Acceleration, Composition, and Transport [EPACT; *von Rosenvinge et al.*, 1995] on the Wind spacecraft, and (f) 5-min average proton intensity in the 14.4–50 MeV energy channels from STA/HET. Note that because the SOHO’s roll angle at this time is 180° , it is possible that SOHO/ERNE missed the first arriving particles. Therefore we used proton data from WIND/EPACT instead of SOHO/ERNE data. The third row of Figure 3 shows the VDA results for the three spacecraft where onset levels of 0.5%, 10% and 10% were used for STA and STB SEPT, and Wind/3DP, and 0.5%, 12% and 15% for STA and STB HET, and Wind/EPACT, respectively.

Finally, Figure 4 first row shows the electron fluxes for the 2013 March 05 event: (a) 5-min average electron intensity in the 50–275 keV energy channels from STB/SEPT, (b) 30-min average electron intensity in the 39–513 keV energy channels from Wind/3DP and (c) 5-min average electron intensity in the 50–275 keV energy channels from STA/SEPT pointing towards the solar direction. The red vertical dashed line in the plot marks the onset time of the associated type III radio burst. Again, the best-connected STA observed the most intense and abrupt increase of SEPs. The maximum intensity of STB/SEPT was two orders of magnitude below that of STA/SEPT, and the rate of the intensity increase was slower. The WIND/3DP intensity was the lowest (\sim three order of magnitude weaker) with the slowest rise. Figure 4 second row shows: (d) 30-min average proton intensity in the 14.4–50 MeV energy channels from STB/HET, (e) 30-min average proton intensity

in the 15.4–57.4 MeV energy channels from SOHO/ERNE, and (f) 5-min average proton intensity in the 14.4–80 MeV energy channels from STA/HET. The third row of Figure 4 shows the VDA results for the three spacecraft where onset levels of 0.5%, 5% and 15% were used for STA and STB SEPT, and Wind/3DP, and 0.5%, 5% and 10% for STA and STB HET, and SOHO/ERNE, respectively.

Table 3 summarizes the energetic electron and proton release times at three spacecraft, where 8.33 minutes have been added to the release times in order to directly compare with electromagnetic emission onsets.

3. CME-shock Front Fitting

We use a forward-modeling technique with a graduated cylindrical shell (GCS) flux-rope model [Thernisien *et al.*, 2009, 2011] plus an oblate spheroid model to fit the CME-shock. The oblate spheroid is obtained by rotating an ellipse about its symmetry axis. The 3D shape and the distance from the solar center of the spheroid are determined by three parameters: semi-minor axes a , b , and the height of the spheroid center h_0 in units of solar radius, or alternative by the height of the leading edge from the solar center h , the eccentricity $e = \sqrt{1 - (a/b)^2}$, and the aspect ratio $\kappa = b/(h - 1)$, where the center of the spheroid $h_0 = h - a$, which can be located above (below or at) the solar surface, as shown in Figure 5. The orientation of the spheroid are determined by the longitude and latitude of its symmetry axis.

In order to find the parameters of the spheroid model, we visually fit the spheroid shock model to near-simultaneous STEREO and SOHO white-light coronagraph, and STEREO and SDO/AIA EUV images. We use EUV wave signatures in the low corona plus coronal signatures in white-light images such as wave-like disturbances and streamer

deflections to constrain the shock model fitting. The GCS model fitting are constrained by CME components, including bright frontal loops or three-part flux rope structures. The forward-modeling constrained with multi-spacecraft observations allowed us to best determine the 3D shape and location of the shock front, and compute the radial and expansion speed of the shock.

Figure 6 presents the CME-shock forward-modeling results and the development of the CME shock and EUV wave for the 2010 August 14 event. Following the solar eruption, a EUV wave was visible in both SDO/AIA and STA/EUVI images. The wave in the SDO AIA images was seen to originate close to AR11099 (N17W52) propagating eastward and it disappeared after $\sim 10:15$ UT. The EUV wave in the STA EUVI images propagated westward and expanded cospatially with the white light disturbances at the first time frame of COR1 at 10:05 UT but diffused away before reaching the magnetic footpoint of STA. No clear disk signature was seen in STB/EUVI images. Rows 1–3 show three different, near-simultaneous views of the CME-shock structure with the oblate spheroid shock model (red wireframe) and the CME flux rope model (green wireframe) superimposed on them at three different times during the eruption. Figure 7 plots the expansion of the fitted shock model as a series of red circular contours superimposed on a Carrington map of 195 Å EUVI images. The contours are plotted in $\sim 5^\circ$ intervals of polar angle θ_p , marking the projections of the shock front at varying heights on the solar disk. The smallest circle is located in the vicinity of the shock nose with $\theta_p \sim 5^\circ$, and the last circle denotes the shock front near the coronal base with $\theta_p = \theta_{max}$. In the figure, the magnetic footpoints of STA, STB and Earth (L1) are marked with red, blue, green dots, along with the location of the CME-shock nose (yellow cross). By plotting such mapping of the

shock front at successive times during the expansion, we are able to find the time when the shock wave arrives at the magnetic footpoint, or the time when the widest part of the shock intercepts with the magnetic field line connecting to each spacecraft. We define the earliest interception time as the magnetic connection time of each spacecraft. Note that we neglect the small difference between the cobpoint location and the magnetic footpoint in the map, given a rotation speed of the Parker spiral field lines of about 14° per day.

The fitting results show that the propagation directions of the shock wave (and FR) was N03W50 (N04W50) at 09:50 UT, S06W50 (S06W50) at 10:15 UT, and S22W45 (S15W45) at 10:50 UT, respectively, indicating that both the shock and CME propagated southward from AR11099 (N17W52) during the eruption, as seen in Figure 6. Assuming the metric type II onset at $\sim 09:52$ UT to be the proxy of the shock formation time, the CME shock intersected the Parker spiral field lines connecting to Earth almost immediately (Figure 7 top panel) at a leading-edge height of $\sim 2.0 R_s$. By interpolating the shock height at two consecutive frames, we found that the the shock wave established the magnetic connection with STB around 10:01 UT when the shock leading edge was $\sim 2.66 R_s$ and with the near-Earth (L1) spacecraft around 10:37 UT at the leading edge of $\sim 6.5 R_s$. As shown in Figure 7 middle panel, the fitted shock front was seen to approach to the STB footpoint at 10:00 UT, with a half width of $\sim 46^\circ$ at the height of $\sim 2.56 R_s$. It expanded to the back side and just passed the STA footpoint around 10:40 UT (bottom panel) with a half width of $\sim 104^\circ$ at $\sim 6.96 R_s$, resulting in an average shock speed of 1283 km/s in the leading-edge direction during its initial expanding phase from 10:10 UT to 10:40 UT and an average lateral expansion rate of $\sim 1.45^\circ/\text{min}$ (297 km/s).

For the 2011 November 03 SEP event, the associate EUV wave was only seen on the solar disk by STB, starting at $\sim 22:10$ UT and disappearing around 22:40 UT before it reached the STB footpoint. The white-light disturbances in COR1 images appeared to track the EUV wave expansion from 22:25 UT to 22:40 UT. The lateral expansion of the CME slows down between 22:45 UT and 22:55 UT and the EUV wave became more diffuse and harder to locate. Figure 8 and Figure 9 present the fitting results for the 2011 November 03 event. The fitting propagation directions for the CME-shock was N06E151 at $\sim 22:25$ UT and 10:15 UT, and N03E152 at $\sim 10:55$ UT, respectively, indicating a nearly radial eruption from its farside flare source (N09E154). Comparing to the 2010 August 14 event, the CME shock exhibited a faster expansion in the lateral direction, as shown from STA and STB views in Figure 8. The shock half width increased from $\sim 31^\circ$ at 22:25 UT to $\sim 148^\circ$ at $\sim 22:55$ UT, resulting in an average expansion rate of $\sim 3.9^\circ/\text{min}$ (~ 794 km/s), which was ~ 2.7 times as fast as that (~ 297 km/s) in the 2010 August 14 event. The shock has passed the STA footpoint at $\sim 22:25$ UT, as seen in the first panel of Figure 9, at $\sim 2.01R_s$. It expanded rapidly to the back side and arrived at the STB footpoint at $\sim 22:52$ UT, and slightly later at L1 footpoint at $\sim 22:55$ UT at $\sim 5.22R_s$. From the third panel in Figure 9, we can clearly see that the fitted shock front reached (passed) the STB (L1) footpoint at 22:55 UT. The average shock speed from 22:25 UT to 22:55 UT was 1248 km/s, which is similar to that in the 2010 August 14 event.

Figure 10 and Figure 11 show the CME-shock fitting results for the 2013 March 05 event. For this event, the associated EUV wave was seen on the disk only in the first frame around 03:25 UT in STEREO EUVI images. The coronal waves and large disturbances

were clearly seen in both COR1 and COR2 white-light images and propagated all the way towards the COR2 field of view at $\sim 06:39$ UT. The fitting propagation directions of the shock (FR) was N08E144 (N03E144) at 03:30 UT, N08E144 (S02E144) at 03:50 UT, and N02E144 (S02E144) at 04:54 UT, respectively, indicating a slightly southward eruption from its farside flare source (N10E144). The shock wave established magnetic connections to STA, STB and L1 at $\sim 03:18$ UT, $\sim 03:42$ UT, and $\sim 03:57$ UT, respectively. Figure 11 show that (top) the fitted shock front already passed the STA footpoint at 03:30 UT with a half width of $\sim 57^\circ$ at $2.64 R_s$ and (middle) passed the STB footpoint and approached the L1 footpoint at 03:55 UT with a half width of $\sim 141^\circ$ at $5.25 R_s$. In Figure 11 bottom panel the fitted shock front is seen to pass the L1 footpoint at 04:54 UT at $\sim 13.6 R_s$ with a half width of $\sim 180^\circ$, i.e., when the shock wave had expanded all the way around the Sun (circumsolar shock). The average radial speed of the shock during the period from 03:30 UT to 04:54 UT was 1523 km/s, which was the highest among the three events and average lateral expansion rate was $\sim 1.48^\circ/\text{min}$ (~ 300 km/s), which was similar to that in the 2010 August 14 event.

Table 4 summarizes the magnetic connection times (MCTs) of the SEP events, i.e., the time when the shock wave established the magnetic connection with each spacecraft, and time delays of the SEP release times relative to MCTs for the three spacecraft.

4. Heights and Speeds of the Shock at Cobpoints at SEP Release Times

If we mark the magnetic intersection cobpoint P on a shock surface by its polar coordinates (R_p, θ_p) , where R_p is the heliocentric distance and θ_p is the polar angle from the ellipse center, as illustrated by Figure 5.

The shock heliocentric distance R_p and speed V_p at any given point P can be computed as a function of θ_p :

$$R_p = \sqrt{x_p^2 + z_p^2}, \quad (3)$$

$$x_p = r_{\theta_p} \cos \theta_p + h_0, z_p = r_{\theta_p} \sin \theta_p, r_{\theta_p} = ab / \sqrt{(b \cos \theta_p)^2 + (a \sin \theta_p)^2} \quad (4)$$

$$V_p = d(R_p)/dt \quad (5)$$

where θ_p can be obtained directly from Figures 7, 9, and 11.

The shock half width is defined as:

$$\omega_{half} = \begin{cases} \sin^{-1}\left(\frac{r_{\theta_p} \sin \theta_p}{R_p}\right), & \text{if } x_p \geq 0 \\ 180^\circ - \sin^{-1}\left(\frac{r_{\theta_p} \sin \theta_p}{R_p}\right), & \text{if } x_p < 0 \end{cases} \quad (6)$$

where P(R_p, θ_p) is on the shock front that has the widest width.

By letting $R_p = 1.12R_s$ and $\theta_p = \theta_{euw}$, we obtain the half width of the shock EUV imprint, i.e., when the shock front sweeps the low corona producing the EUV imprint [Patsourakos and Vourlidas, 2012]. As shown in Figure 12, two cases are present with $\omega \leq 90^\circ$ ($x_p \geq 0$) and $\omega > 90^\circ$ ($x_p < 0$). Note that the shock half width is equal to the half width of the shock EUV imprint when $x_p < 0$ but they can be different when $x_p > 0$. Also, Once the shock expands beyond certain solar radii and the shock front no longer intersects the low corona, θ_p in Eq. (6) should be replaced by θ_{corona} , i.e., the coronal imprint of the shock wave sweeping material at the base of the streamers at height $> 1.12R_s$. When a shock expands all the way around the Sun, i.e., becomes a circumsolar shock, θ_{corona} reaches its maximum value of 180° .

Figure 13 presents the shock height (left) and speed (middle) at the cobpoints of the three spacecraft, the half width and maximum θ_p (right) as a function of time for the three events. In the figure, the shock leading-edge heliocentric distance and speed (black

solid curve) is overplotted along with the shock cobpoint heights and speeds. Vertical dashed-lines in the plot mark the SEP electron release times for the three spacecraft. The first row in Figure 13 shows the results for the 2010 August 14 event. For this event, the shock is best connected with L1 ($CA = 4^\circ$) and relatively well connected with STB ($CA = 48^\circ$). The shock height and speed at the L1 (STB) cobpoint is very close to (slightly lower than) the height and speed in the leading-edge direction. The shock speed at the L1 cobpoint (red diamonds) increased rapidly to ~ 970 km/s by the Earth (L1) electron (e^-) release time of $\sim 10:05$ UT, and the speed at the STB cobpoint (green diamonds) increased to ~ 964 km/s by the STB e^- release time of $\sim 10:14$ UT. The shock speed at the STA cobpoint ($CA = 92^\circ$) (blue diamonds), however, increased much more slowly and was only ~ 471 km/s by the STA e^- release time of $\sim 10:46$ UT. The polar angles at the three cobpoints at their SPR times were $\sim 10^\circ$, $\sim 97^\circ$ and $\sim 149^\circ$, respectively, and the shock half width had increased from $\sim 49^\circ$ to $\sim 113^\circ$. If a direct connection to the shock front was the source of the first particles, this suggests that the particle acceleration would have occurred both near the nose and at the flank of the shock even when the shock flank travelled to the backside of the Sun. The heliocentric distances of cobpoints for L1, STB and STA at the e^- release times were $2.94 R_S$, $2.78 R_S$ and $2.22 R_S$, respectively.

For the 2011 November 03 event (Figure 13 second row), the shock is best connected with STA ($CA = 11^\circ$) and the shock speed at STA cobpoint increased to ~ 1036 km/s by the electron release time of $\sim 22:29$ UT, which is similar to the L1 cobpoint speed in the 2010 August 14 event. The shock speeds at STB ($CA = 130^\circ$) and L1 ($CA = 135^\circ$) cobpoints, however, were relatively small ~ 590 km/s at the e^- release time of $\sim 23:00$ UT, which is slightly larger than the STA cobpoint speed in the 2010 August 14 event.

The acceleration of SEPs observed at STA have occurred near the shock nose with $\theta_p = \sim 31^\circ$, and the acceleration of SEPs observed at STB and L1 may have occurred at the backside with $\theta_p = \sim 160^\circ$ at $\sim 23:00$ UT. During the initial expanding phase from 22:30 UT to 23:00 UT, the shock half width increased from $\sim 41^\circ$ to $\sim 158^\circ$, yielding a much faster expansion speed than the 2010 August 14 event. The shock cobpoint heights at their electron SPR times were $\sim 2.34 R_s$ for STA, $\sim 2.13 R_s$ and $\sim 1.6 R_s$ for STB and L1, respectively.

For the 2013 March 05 event (Figure 13 third row), the SEP source is again best connected with STA ($CA = 14^\circ$) and poorly connected with STB ($CA = 94^\circ$) and L1 ($CA = 152^\circ$). The shock speed at STA cobpoint was ~ 892 km/s around the electron SPR time of $\sim 03:30$ UT, which was slightly smaller than that in the 2011 November 3 event, but increased continuously to ~ 1530 km/s by $\sim 03:50$ UT. The cobpoint height of $2.47 R_s$ at the STA SPR time was in the similar range as those in the other two events. The acceleration of SEPs observed at STB could have occurred at the backside of the Sun with θ_p of $\sim 127^\circ$ and R_p of $\sim 5.22 R_s$, where the CME-shock had evolved to a circumsolar shock at the STB e- SPR time of $\sim 04:30$ UT, if we assume a direct shock connection to be the particle source. By the L1 SPR time of $\sim 08:25$ UT, the shock has propagated beyond the COR2 field of view with a leading-edge height of $> \sim 0.1$ AU, where we are no longer able to trace the cobpoint R_p , V_p and θ_p .

As shown in Table 4, the electron SPR times are around 4 – 17 min delayed from their magnetic connection times for most of the SEP events except SEPs observed at L1 and at STB on 2013 March 05. The proton SPR times are around 15 to 37 min after their magnetic connection times, again with exceptions for the STB and L1 SEPs on 2013

March 05. In Table 5, we summarize the height and speed of the shock at the cobpoints at the SPR times of electrons and protons, respectively. Table 5 columns 3 - 5 list the shock height at the cobpoints of STA, near-Earth (L1) spacecraft and STB. Columns 6 - 8 list the shock speed of the cobpoints of the three spacecraft and columns 9 - 11 list the polar angles of the cobpoints of the three spacecraft. Columns 12 - 14 present the shock half width at the SEP SPR times. From Table 5 we can see that the shock heights at the cobpoints at proton SPR times are ~ 0.3 to $1.88 R_s$ higher than those at electron release times, except for the 2013 March 05 SEP at STB. The shock speeds at the cobpoints at proton SPR times are < 200 km/s larger than those at electron release times except for the 2011 November 03 SEP at STB and L1, which have similar speeds (< 22 km/s difference) at both electron and proton release times.

5. Summary and Discussion

5.1. Summary

Using a forward-modeling technique, we fit the FR and spheroid shock model to STEREO white-light coronagraph and EUV images, SOHO white-light coronagraph and SDO/AIA EUV images for the three longitudinally widespread SEP events. The forward-modeling constrained with multi-spacecraft observations allowed us to best determine the 3D shape and location of the shock front, and compute the shock height and speed at the cobpoint of each observing spacecraft. The main results are summarized below.

1) The SEPs observed at the well-connected spacecraft are shown to be released at a relatively narrow range of heights from $\sim 2.34 R_s$ to $3.43 R_s$ with the shock speeds ranging from ~ 892 km/s to 1222 km/s for the three events. The SEPs observed at the poorly-connected spacecraft when the shock acceleration may have occurred at the backside of

the Sun with $\theta_p > \sim 127^\circ$ have a much wider release height range from $\sim 1.45 R_s$ to $8.06 R_s$ with the shock speeds ranging from ~ 471 km/s to 1000 km/s. No clear EUV wave signatures on the disk were seen to reach the magnetic footpoints connecting to the poorly-connected spacecraft in all the three SEP events.

2) For the 2010 August 14 event, the shock established the magnetic connection to L1, STB and STA at ~ 1.12 to $1.2 R_s$ around 09:52 UT, 10:01 UT and 10:37 UT, respectively. The SEP electron and proton release times were around 9 to 29 min delayed from their magnetic connection times. The shock speeds at the cobpoints of L1 and STB were > 900 km/s and the particle accelerations are suggested to occur near the nose and at flank of the shock with $\theta_p = 10^\circ$ and 97° , respectively. Significant electron anisotropies were observed for both the Wind and STB SEP electrons by *Dresing et al.* [2014], supporting the scenario that each source of the SEP increases at L1 and STB was a direct connection to the shock front. The SEPs observed at STA, however, with a small cobpoint shock speed (~ 471 km/s) and showing no significant anisotropy [*Dresing et al.*, 2014], may be caused by other mechanisms (see discussion below), such as cross-field diffusion.

3) The shock wave of the 2011 November 03 SEP event had a faster expansion speed than that of the 2010 August 14 event. The shock magnetic connection times to STA, STB, and L1 were around 22:17 UT, 22:52 UT and 22:55 UT, respectively. The observed SEP electron and proton release times at STA, STB and L1 spacecraft were around 4 to 37 min delayed from their magnetic connection times. For this event, the magnetic connection with both STB and L1 occurred when the shock flank was far backside of the Sun ($\theta_p > 158^\circ$). However, the SEP intensities at all three spacecraft show an abrupt rise and long-lasting anisotropy [*Gómez-Herrero et al.*, 2015]. Therefore, we find the

suggestion of *Gómez-Herrero et al.* [2015] that the most likely cause of the SEP increases at all three spacecraft was a direct connection to the shock front reasonable.

4) The 2013 March 05 SEP event had the highest shock leading-edge speed, which is consistent with the highest STA SEP intensity peak observed among the three events. For this event, the magnetic connection times for STA, STB, and L1 are 03:18 UT, 03:42 UT and 03:57 UT, respectively. The SEP electron and proton release time at STA was delayed ~ 11 and 15 min from the magnetic connection time, which is similar to the other two events. However, the SEP intensities observed by the STB and L1 spacecraft had a very slow rise with SPR time delays of ~ 1 hr and ~ 5 hr, showing almost no anisotropy, indicating that the observed SEP increases were likely caused by cross-field transport and/or other mechanisms.

5.2. Circumsolar Shocks

Uchida [1968] modeled a linear fast-mode magnetohydrodynamics (MHD) wave propagating in the corona. He found that the disturbance moves along rays and curves into regions of a reduced Alfvén speed, resulting in a wave front that should ideally look spheroid in its geometry. Recently, *Afanasyev and Uralov* [2011] used non-linear theory to describe the evolution of a coronal shock wave and indicated that the shock wave front should also look spheroid-like. However, there is no direct proof that circumsolar shocks exist in the high corona. Our fitting results indicate that an oblate spheroid model is best to fit the CME-shock front and EUV wave during its early evolution. Once the shock has expanded beyond a distance of a few solar radii, the EUV wave will disappear. For such cases, we fitted the spheroid shock model to coronal signatures seen in the white-light images, including wave-like disturbances and deflected streamers. The observed coronal

imprints can be caused 1) by the similar mechanisms and kinematics as EUV imprints, i.e., they are produced when the shock wave sweeps the materials at the base of the streamer it's pushing into and 2) by the fast-mode MHD shock wave in the extended corona or the shock wave followed by blast-type waves that freely propagate behind a piston-shock driven by the expanding flank of CMEs [e.g. *Patsourakos and Vourlidas, 2009; Kwon et al., 2013; Kwon and Vourlidas, 2017; Liu et al., 2017*]. On the other hand, there is uncertainty in the white-light images whether such coronal imprints are due to projection effects from overlapping disturbances at greater heights or they are caused by an actual backside shock wave that has expanded all the way around the Sun. The spheroid model assumes that the shock waves can expand all the way around the Sun unless they are intersecting with the solar surface. Such assumption may bring uncertainties to the shock fitting results. First, if the shock waves are weak and stop at height greater than $1.12R_s$, then θ_{max} in eq. (6) will be $< 180^\circ$ which will result in a delayed magnetic connection time. For example, for the 2010 August 14 event, if the shock stopped at the streamer base in COR1 at height of $\sim 3.6R_s$ at $\sim 10:50$ UT (Figure 6h), the shock extent would be smaller and it would not establish the magnetic connection with STA until $\sim 11:08$ UT. Second, if the observed coronal wave at the wake of the shock is associated with the freely propagating blast-type wave, it may become weak quickly and not be able to accelerate SEPs, especially when CMEs have traveled outward into outer corona, e.g., as shown in Figure 10 (g)–(i), where the CME shock height had reached $\sim 14R_s$. Recently, *Kwon and Vourlidas [2017]* have showed that a CME can drive piston-type shock in the inner corona due to strong lateral expansion but the flank shock can quickly devolve into blast-type waves as the CME moves outward. *Liu et al. [2017]* studied the 2012 July 23 eruption and

showed evidence of the backward expansion of the shock front into the side of the Sun opposite to the solar source location and the CME propagation direction. However, they also suggest that even though the shock at the nose of the CME likely persists far into the IP space, the shock more likely decays at the wake some time after the expansion in the lateral direction ceases. Finally, when CMEs propagate in the inhomogeneous ambient medium with non-symmetric expansion, as shown in Figures 6 (g) and (h) where the CME-driven shock had much weaker expansion at the southern flank, the spheroid model can overestimate the shock extent at some position angles. For such cases the circumsolar shock may not be a correct assumption and may overestimate the actual longitudinal extent of the shock.

5.3. EUV or Coronal Waves

EUV or coronal waves can be driven by and closely track the lateral expanding flank of CMEs [*Krucker et al.*, 1999; *Rouillard et al.*, 2012], especially when the expansion speed is greater than the fast-mode speed (400–500 km/s) of the ambient plasma, thereby producing quasi-perpendicular shocks that accelerate particles. We would like to note that recent SDO observations confirm the existence of two EUV waves: a faster wave ahead of another slower wave [see the review by *Chen*, 2016]. The faster-propagating EUV wave most likely is the fast-mode MHD shock, whereas the nature of the slower-propagating wave is still uncertain. It is also possible that the shock wave that is initially driven by the laterally expanding flanks of the CME later becomes a freely propagating disturbance when the CME ceases expanding laterally. As fast and widespread EUV or coronal waves extend to the foot points of field lines connected to the widely-separated spacecraft, they may produce longitudinally widely extending SEP events. However, *Nitta*

et al. [2013] noted that not all longitudinally wide SEP events are necessarily associated with EUV waves. They listed other possible processes which might contribute to the particle longitudinal transport, such as, particle injections from sympathetic flares or the existing large-scale magnetic loops that might guide SEPs to locations far from the original solar event [Schrijver *et al.*, 2013]. In addition, Miteva *et al.* [2014] conducted a survey for 179 SEP events during Solar Cycle 23 and found that the EIT waves could not explain the earlier onset of near-relativistic electrons with weak anisotropy in some eastern SEP events. They suggested cross-field particle transport due to diffusion or due to field-line wandering combined with spatially extended shocks to be the source of such eastern events.

5.4. Cross-field diffusion in the solar wind

Cross-field diffusion in the solar wind is another likely cause for the widespread SEP events. Giacalone and Jokipii [2012] proposed a diffusive model to explain the interplanetary longitudinal transport of energetic ions from impulsive solar flares. With regard to the interplanetary magnetic field, they found that perpendicular diffusion can reproduce the recent multi-spacecraft observations [e.g. Wiedenbeck *et al.*, 2013] if a sufficiently large value of the ratio of the perpendicular and parallel diffusion coefficients, $\kappa_{per}/\kappa_{para}$, is assumed. Dröge *et al.* [2010] used ratio 0.01 in their simulations and found that SEPs at 1 AU spread over azimuthal range of 90° . However, the amount of perpendicular diffusion of particles is still under debate at present. While single spacecraft observations of sharp cross-field gradients (dropouts) in the intensity profiles of low-energy ions in impulsive solar particle events indicated ratios of the order of $\sim 10^{-4}$ [e.g. Mazur *et al.*, 2000; Dröge *et al.*, 2010], the modulation of galactic cosmic rays and observations of Jovian electrons

have suggested a ratio of $\sim 10^{-2}$ [Conlon, 1978]. Recent numerical simulations also supported larger values of ~ 0.02 to 0.05 [e.g. Matthaeus *et al.*, 2003]. In a recent study, the SEP profiles at the three spacecraft for the 2010 August 14 SEP event have been reproduced by the SEP transport model that includes cross-field diffusion in the IP space, and suggested that SEPs reached STA mostly via cross-field diffusion [Lario *et al.*, 2017]. On the other hand, Laitinen *et al.* [2016] developed a model where field line meandering due to plasma turbulence facilitates the wide spread of particles across field lines at the early phase of the event. Only later in the event, the cross-field transport becomes diffusive. However, Tooprakai *et al.* [2016] used a different method of full trajectory simulations to model the cross-field diffusion and found narrower distributions for particles at 1 AU than Laitinen *et al.* [2016]. They note that in their simulations the angular extent of field line meandering is limited by trapping boundaries forming in the turbulence.

5.5. Conclusion

Our fitting results support that the SEPs observed at the three spacecraft on 2011 November 03, STB and L1 on 2010 August 14, and the 2013 March 5 SEP event at STA are accelerated by a direct connection to the CME-shock, which is consistent with the significant anisotropies observed at these locations. Cross-field diffusion is the likely cause for the 2010 August 14 SEP event observed by STA and the 2013 March 05 SEPs observed by STB and L1 spacecraft, which were characterized by weak anisotropy of the electrons, resulting from the scattering during the transport across the magnetic field lines [e.g. Dresing *et al.*, 2012; Qin *et al.*, 2013; Qin and Wang, 2015; Wang *et al.*, 2012]. Otherwise, the wide longitudinal spread of these SEP increases would require an existence of a circumsolar shock, which may not be a correct assumption in the high corona and

heliosphere. Further quantitative analyses on combined effects of the spatially extended shock acceleration with a prolonged duration and cross-diffusion transport are needed in the future modeling.

Acknowledgments. The authors would like to thank the support of STEREO, SOHO, WIND and ACE teams. The STEREO SECCHI data are produced by a consortium of RAL (UK), NRL (USA), LMSAL (USA), GSFC (USA), MPS (Germany), CSL (Belgium), IOTA (France), and IAS (France). The SOHO LASCO data are produced by a consortium of the Naval Research Laboratory (USA), Max-Planck-Institut für Aeronomie (Germany), Laboratoire d’Astronomie (France), and the University of Birmingham (UK). SOHO Energetic and Relativistic Nuclei and Electron instrument (ERNE) data were obtained from: http://www.srl.utu.fi/erne_data/datafinder/df.shtml; STEREO High Energy Telescope (HET) data were obtained from: http://www.srl.caltech.edu/STEREO/Public/HET_public.html; STEREO High Energy Telescope (LET) data were obtained from: http://www.srl.caltech.edu/STEREO/Public/LET_public.html; STEREO Solar Electron Proton Telescope data (SEPT) were obtained from: <http://www2.physik.uni-kiel.de/STEREO/index.php?doc=data>; and Wind/3DP and ACE/EPAM proton and electron data were obtained from http://cdaweb.gsfc.nasa.gov/istp_public/. This work was supported by NASA LWS TR&T program NNX15AB70G. PM was partially supported by NASA grant NNX15AB77G and NSF grant AGS-1358274.

References

Afanasyev, A. N., and A. M. Uralov (2011), Coronal Shock Waves, EUV Waves, and Their Relation to CMEs. II. Modeling MHD Shock Wave Propagation Along the Solar

- Surface, Using Nonlinear Geometrical Acoustics, *Solar Phys.*, *273*, 479–491, doi:10.1007/s11207-011-9730-9.
- Brueckner, G. E., et al. (1995), The Large Angle Spectroscopic Coronagraph (LASCO), *Solar Phys.*, *162*, 357–402, doi:10.1007/BF00733434.
- Cane, H. V., and W. C. Erickson (2003), Energetic particle propagation in the inner heliosphere as deduced from low-frequency (<100 kHz) observations of type III radio bursts, *Journal of Geophysical Research (Space Physics)*, *108*, 1203, doi:10.1029/2002JA009488.
- Chen, P. F. (2016), Global Coronal Waves, *Washington DC American Geophysical Union Geophysical Monograph Series*, *216*, 381–394, doi:10.1002/9781119055006.ch22.
- Cliver, E. W., S. W. Kahler, D. F. Neidig, H. V. Cane, I. G. Richardson, M. B. Kallenrode, and G. Wibberenz (1995), Extreme “Propagation” of Solar Energetic Particles, *International Cosmic Ray Conference*, *4*, 257.
- Conlon, T. F. (1978), The interplanetary modulation and transport of Jovian electrons, *J. Geophys. Res.*, *83*, 541–552, doi:10.1029/JA083iA02p00541.
- Domingo, V., B. Fleck, and A. I. Poland (1995), SOHO: The Solar and Heliospheric Observatory, *Space Sci. Rev.*, *72*, 81–84, doi:10.1007/BF00768758.
- Dresing, N., R. Gómez-Herrero, A. Klassen, B. Heber, Y. Kartavykh, and W. Dröge (2012), The Large Longitudinal Spread of Solar Energetic Particles During the 17 January 2010 Solar Event, *Solar Phys.*, *281*, 281–300, doi:10.1007/s11207-012-0049-y.
- Dresing, N., R. Gómez-Herrero, B. Heber, A. Klassen, O. Malandraki, W. Dröge, and Y. Kartavykh (2014), Statistical survey of widely spread out solar electron events observed with STEREO and ACE with special attention to anisotropies, *Astron. Astrophys.*, *567*, A27, doi:10.1051/0004-6361/201423789.

Dröge, W., Y. Y. Kartavykh, B. Klecker, and G. A. Kovaltsov (2010), Anisotropic Three-Dimensional Focused Transport of Solar Energetic Particles in the Inner Heliosphere, *Astrophys. J.*, *709*, 912–919, doi:10.1088/0004-637X/709/2/912.

Giacalone, J., and J. R. Jokipii (2012), The Longitudinal Transport of Energetic Ions from Impulsive Solar Flares in Interplanetary Space, *Astrophys. Lett.*, *751*, L33, doi:10.1088/2041-8205/751/2/L33.

Gómez-Herrero, R., et al. (2015), Circumsolar Energetic Particle Distribution on 2011 November 3, *Astrophys. J.*, *799*, 55, doi:10.1088/0004-637X/799/1/55.

Howard, R. A., et al. (2008), Sun Earth Connection Coronal and Heliospheric Investigation (SECCHI), *Space Sci. Rev.*, *136*, 67–115, doi:10.1007/s11214-008-9341-4.

Kallenrode, M.-B., G. Wibberenz, H. Kunow, R. Müller-Mellin, V. Stolpovskii, and N. Kontor (1993), Multi-spacecraft observations of particle events and interplanetary shocks during November/December 1982, *Solar Phys.*, *147*, 377–410, doi:10.1007/BF00690726.

Krucker, S., D. E. Larson, R. P. Lin, and B. J. Thompson (1999), On the Origin of Impulsive Electron Events Observed at 1 AU, *Astrophys. J.*, *519*, 864–875, doi:10.1086/307415.

Kwon, R.-Y., and A. Vourlidas (2017), Investigating the Wave Nature of the Outer Envelope of Halo Coronal Mass Ejections, *Astrophys. J.*, *836*, 246, doi:10.3847/1538-4357/aa5b92.

Kwon, R.-Y., L. Ofman, O. Olmedo, M. Kramar, J. M. Davila, B. J. Thompson, and K.-S. Cho (2013), STEREO Observations of Fast Magnetosonic Waves in the Extended Solar Corona Associated with EIT/EUV Waves, *Astrophys. J.*, *766*, 55, doi:10.1088/

0004-637X/766/1/55.

Laitinen, T., K. Huttunen-Heikinmaa, and E. Valtonen (2010), On the Effect of Pre-event Background in Determining Solar Particle Event Onset, *Twelfth International Solar Wind Conference, 1216*, 249–252, doi:10.1063/1.3395847.

Laitinen, T., A. Kopp, F. Effenberger, S. Dalla, and M. S. Marsh (2016), Solar energetic particle access to distant longitudes through turbulent field-line meandering, *Astron. Astrophys.*, *591*, A18, doi:10.1051/0004-6361/201527801.

Lario, D., N. E. Raouafi, R.-Y. Kwon, J. Zhang, R. Gómez-Herrero, N. Dresing, and P. Riley (2014), The Solar Energetic Particle Event on 2013 April 11: An Investigation of its Solar Origin and Longitudinal Spread, *Astrophys. J.*, *797*, 8, doi:10.1088/0004-637X/797/1/8.

Lario, D., et al. (2016), Longitudinal Properties of a Widespread Solar Energetic Particle Event on 2014 February 25: Evolution of the Associated CME Shock, *Astrophys. J.*, *819*, 72, doi:10.3847/0004-637X/819/1/72.

Lario, D., et al. (2017), The Solar Energetic Particle Event of 2010 August 14: Connectivity with the Solar Source Inferred from Multiple Spacecraft Observations and Modeling, *Astrophys. J.*, *838*, 51, doi:10.3847/1538-4357/aa63e4.

Lemen, J. R., et al. (2012), The Atmospheric Imaging Assembly (AIA) on the Solar Dynamics Observatory (SDO), *Solar Phys.*, *275*, 17–40, doi:10.1007/s11207-011-9776-8.

Lin, R. P., et al. (1995), A Three-Dimensional Plasma and Energetic Particle Investigation for the Wind Spacecraft, *Space Sci. Rev.*, *71*, 125–153, doi:10.1007/BF00751328.

Lintunen, J., and R. Vainio (2004), Solar energetic particle event onset as analyzed from simulated data, *Astron. Astrophys.*, *420*, 343–350, doi:10.1051/0004-6361:20034247.

- Liu, Y. D., H. Hu, B. Zhu, J. G. Luhmann, and A. Vourlidas (2017), Structure, Propagation, and Expansion of a CME-driven Shock in the Heliosphere: A Revisit of the 2012 July 23 Extreme Storm, *Astrophys. J.*, *834*, 158, doi:10.3847/1538-4357/834/2/158.
- Malandraki, O. E., et al. (2012), Scientific Analysis within SEPServer - New Perspectives in Solar Energetic Particle Research: The Case Study of the 13 July 2005 Event, *Solar Phys.*, *281*, 333–352, doi:10.1007/s11207-012-0164-9.
- Matthaeus, W. H., G. Qin, J. W. Bieber, and G. P. Zank (2003), Nonlinear Collisionless Perpendicular Diffusion of Charged Particles, *Astrophys. Lett.*, *590*, L53–L56, doi:10.1086/376613.
- Mazur, J. E., G. M. Mason, J. R. Dwyer, J. Giacalone, J. R. Jokipii, and E. C. Stone (2000), Interplanetary Magnetic Field Line Mixing Deduced from Impulsive Solar Flare Particles, *Astrophys. Lett.*, *532*, L79–L82, doi:10.1086/312561.
- Mewaldt, R. A., et al. (2008), The Low-Energy Telescope (LET) and SEP Central Electronics for the STEREO Mission, *Space Sci. Rev.*, *136*, 285–362, doi:10.1007/s11214-007-9288-x.
- Miteva, R., K.-L. Klein, I. Kienreich, M. Temmer, A. Veronig, and O. E. Malandraki (2014), Solar Energetic Particles and Associated EIT Disturbances in Solar Cycle 23, *Solar Phys.*, *289*, 2601–2631, doi:10.1007/s11207-014-0499-5.
- Müller-Mellin, R., S. Böttcher, J. Falenski, E. Rode, L. Duvet, T. Sanderson, B. Butler, B. Johlander, and H. Smit (2008), The Solar Electron and Proton Telescope for the STEREO Mission, *Space Sci. Rev.*, *136*, 363–389, doi:10.1007/s11214-007-9204-4.
- Nitta, N. V., C. J. Schrijver, A. M. Title, and W. Liu (2013), Large-scale Coronal Propagating Fronts in Solar Eruptions as Observed by the Atmospheric Imaging Assembly

- on Board the Solar Dynamics Observatory—an Ensemble Study, *Astrophys. J.*, *776*, 58, doi:10.1088/0004-637X/776/1/58.
- Patsourakos, S., and A. Vourlidas (2009), “Extreme Ultraviolet Waves” are Waves: First Quadrature Observations of an Extreme Ultraviolet Wave from STEREO, *Astrophys. Lett.*, *700*, L182–L186, doi:10.1088/0004-637X/700/2/L182.
- Patsourakos, S., and A. Vourlidas (2012), On the Nature and Genesis of EUV Waves: A Synthesis of Observations from SOHO, STEREO, SDO, and Hinode (Invited Review), *Solar Phys.*, *281*, 187–222, doi:10.1007/s11207-012-9988-6.
- Prise, A. J., L. K. Harra, S. A. Matthews, D. M. Long, and A. D. Aylward (2014), An Investigation of the CME of 3 November 2011 and Its Associated Widespread Solar Energetic Particle Event, *Solar Phys.*, *289*, 1731–1744, doi:10.1007/s11207-013-0435-0.
- Qin, G., and Y. Wang (2015), Simulations of a Gradual Solar Energetic Particle Event Observed by Helios 1, Helios 2, and IMP 8, *Astrophys. J.*, *809*, 177, doi:10.1088/0004-637X/809/2/177.
- Qin, G., Y. Wang, M. Zhang, and S. Dalla (2013), Transport of Solar Energetic Particles Accelerated by ICME Shocks: Reproducing the Reservoir Phenomenon, *Astrophys. J.*, *766*, 74, doi:10.1088/0004-637X/766/2/74.
- Richardson, I. G., et al. (2014), > 25 MeV Proton Events Observed by the High Energy Telescopes on the STEREO A and B Spacecraft and/or at Earth During the First Seven Years of the STEREO Mission, *Solar Phys.*, *289*, 3059–3107, doi:10.1007/s11207-014-0524-8.
- Rouillard, A. P., et al. (2012), The Longitudinal Properties of a Solar Energetic Particle Event Investigated Using Modern Solar Imaging, *Astrophys. J.*, *752*, 44, doi:10.1088/

0004-637X/752/1/44.

Schrijver, C. J., A. M. Title, A. R. Yeates, and M. L. DeRosa (2013), Pathways of Large-scale Magnetic Couplings between Solar Coronal Events, *Astrophys. J.*, *773*, 93, doi:10.1088/0004-637X/773/2/93.

Thernisien, A., A. Vourlidas, and R. A. Howard (2009), Forward Modeling of Coronal Mass Ejections Using STEREO/SECCHI Data, *Solar Phys.*, *256*, 111–130, doi:10.1007/s11207-009-9346-5.

Thernisien, A., A. Vourlidas, and R. A. Howard (2011), CME reconstruction: Pre-STEREO and STEREO era, *Journal of Atmospheric and Solar-Terrestrial Physics*, *73*, 1156–1165, doi:10.1016/j.jastp.2010.10.019.

Tooprakai, P., A. Seripienlert, D. Ruffolo, P. Chuychai, and W. H. Matthaeus (2016), Simulations of Lateral Transport and Dropout Structure of Energetic Particles from Impulsive Solar Flares, *Astrophys. J.*, *831*, 195, doi:10.3847/0004-637X/831/2/195.

Torsti, J., et al. (1995), Energetic Particle Experiment ERNE, *Solar Phys.*, *162*, 505–531, doi:10.1007/BF00733438.

Tylka, A. J., C. M. S. Cohen, W. F. Dietrich, S. Krucker, R. E. McGuire, R. A. Mewaldt, C. K. Ng, D. V. Reames, and G. H. Share (2003), Onsets and Release Times in Solar Particle Events, *International Cosmic Ray Conference*, *6*, 3305.

Uchida, Y. (1968), Propagation of Hydromagnetic Disturbances in the Solar Corona and Moreton's Wave Phenomenon, *Solar Phys.*, *4*, 30–44, doi:10.1007/BF00146996.

Vainio, R., et al. (2013), The first SEP Server event catalogue ~68-MeV solar proton events observed at 1 AU in 1996-2010, *Journal of Space Weather and Space Climate*, *3*(27), A12, doi:10.1051/swsc/2013030.

von Rosenvinge, T. T., et al. (1995), The Energetic Particles: Acceleration, Composition, and Transport (EPACT) investigation on the WIND spacecraft, *Space Sci. Rev.*, *71*, 155–206, doi:10.1007/BF00751329.

von Rosenvinge, T. T., et al. (2008), The High Energy Telescope for STEREO, *Space Sci. Rev.*, *136*, 391–435, doi:10.1007/s11214-007-9300-5.

Wang, Y., G. Qin, and M. Zhang (2012), Effects of Perpendicular Diffusion on Energetic Particles Accelerated by the Interplanetary Coronal Mass Ejection shock, *Astrophys. J.*, *752*, 37, doi:10.1088/0004-637X/752/1/37.

Wiedenbeck, M. E., G. M. Mason, C. M. S. Cohen, N. V. Nitta, R. Gómez-Herrero, and D. K. Haggerty (2013), Observations of Solar Energetic Particles from ^3He -rich Events over a Wide Range of Heliographic Longitude, *Astrophys. J.*, *762*, 54, doi:10.1088/0004-637X/762/1/54.

Wuelser, J.-P., et al. (2004), EUVI: the STEREO-SECCHI extreme ultraviolet imager, in *Telescopes and Instrumentation for Solar Astrophysics, Society of Photo-Optical Instrumentation Engineers (SPIE) Conference Series*, vol. 5171, edited by S. Fineschi and M. A. Gummin, pp. 111–122, doi:10.1117/12.506877.

Xie, H., P. Mäkelä, N. Gopalswamy, and O. C. St. Cyr (2016), Energy dependence of SEP electron and proton onset times, *Journal of Geophysical Research (Space Physics)*, *121*, 6168–6183, doi:10.1002/2015JA021422.

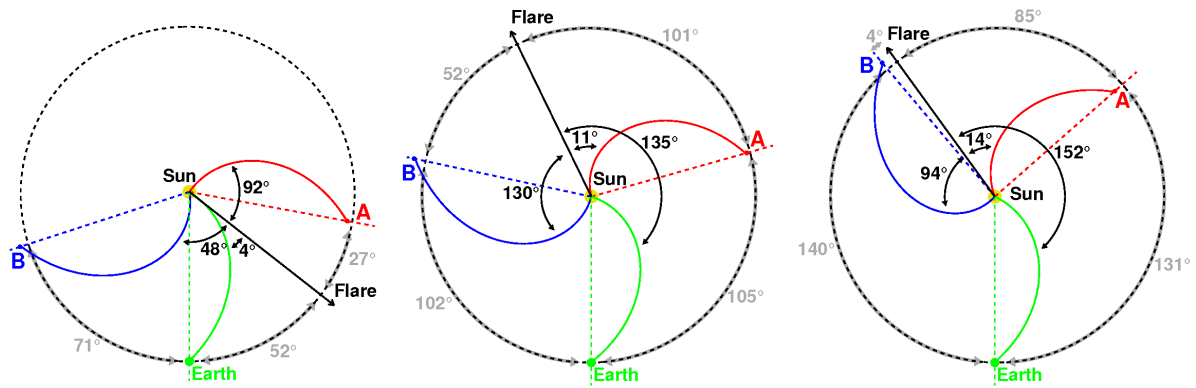


Figure 1. Overview of the three SEP events on August 14, 2010, November 03, 2011, and March 05, 2013 (from left to right). The locations and magnetic field connections to the Sun for each spacecraft together with the locations of the SEP solar sources (flares). The red, blue, and green spots mark the locations of STA, STB, and near-Earth (L1) spacecraft (i.e., SOHO, ACE and Wind). The colored spirals are the nominal Parker field lines connecting the spacecraft to the Sun.

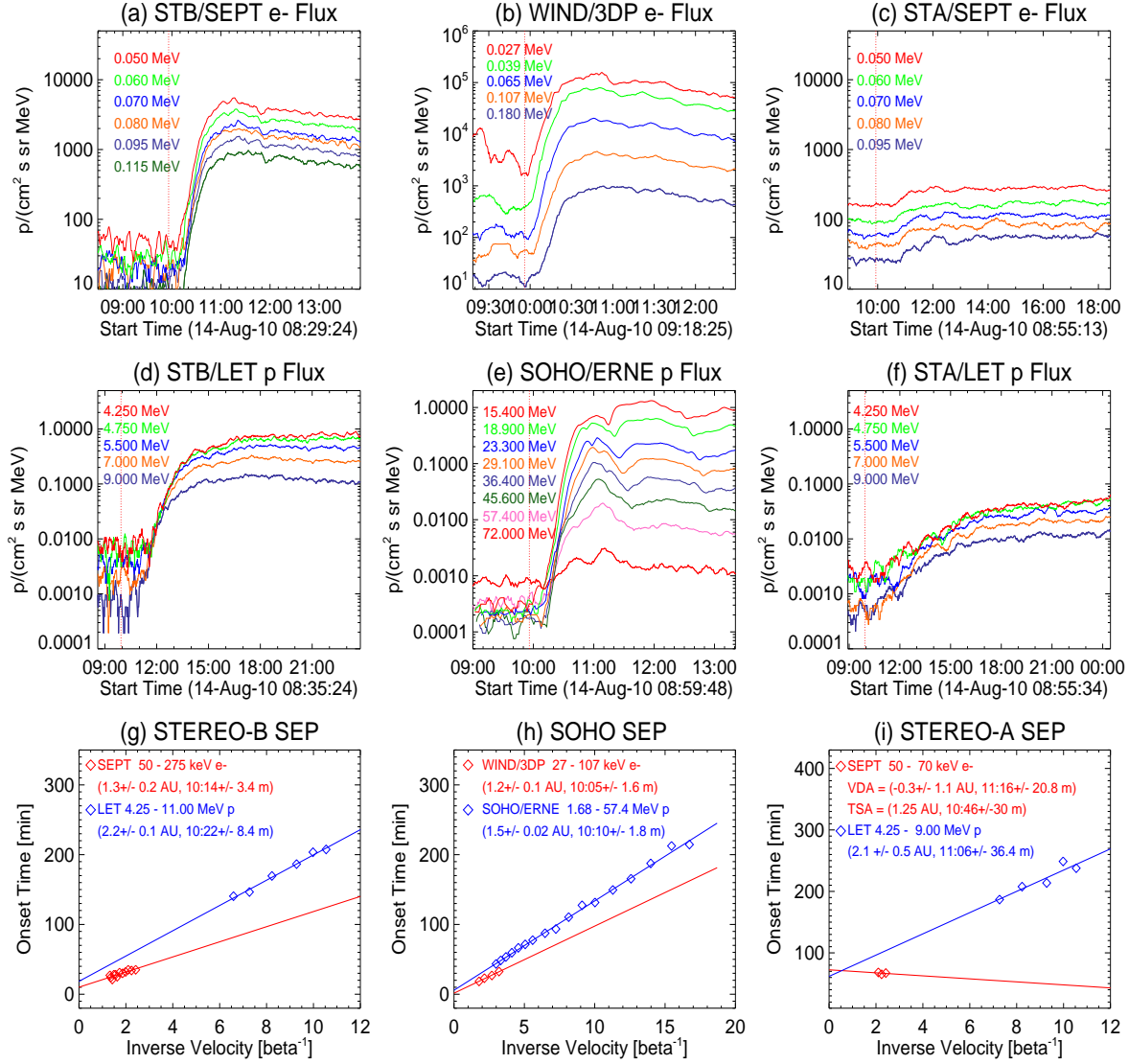


Figure 2. Electron and proton fluxes of the 2010 August 14 SEP event: (a)-(c) electron data from STB/SEPT, WIND/3DP, and STA/SEPT, (d)-(f) proton data from STB/LET, SOHO/ERNE and STA/LET and (g)-(i) the VDA results for the three locations. The red vertical dashed lines in the first and second rows mark the onset time of the associated type III radio burst.

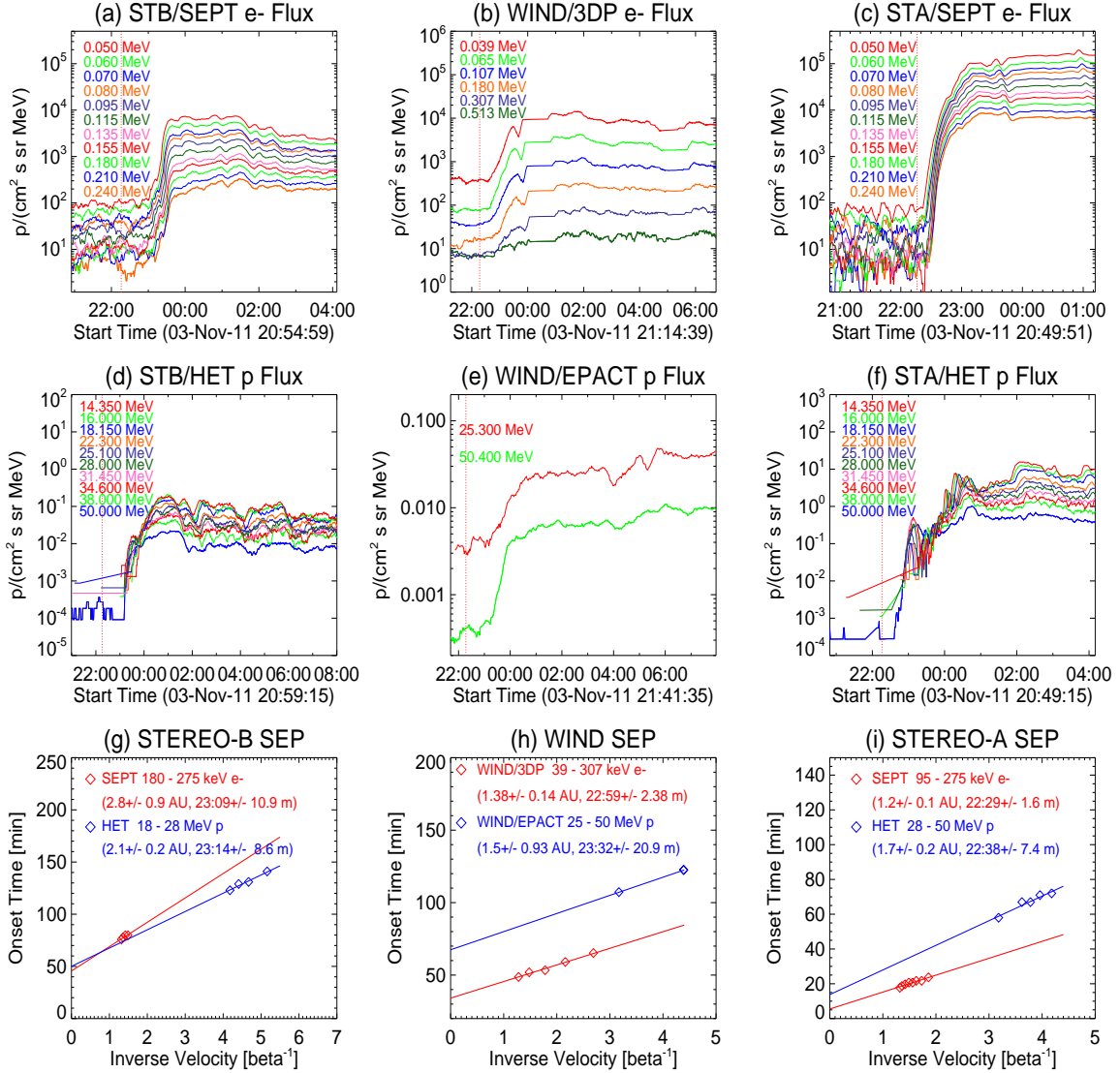


Figure 3. Electron and proton fluxes of the 2011 November 3 SEP event: (a)-(c) electron data from STB/SEPT, WIND/3DP and STA/SEPT, (d)-(f) proton data from STB/HET, WIND/EPACT and STA/HET and (g)-(i) the VDA results for the three locations. The red vertical dashed lines in the first and second rows mark the onset time of the associated type III radio burst.

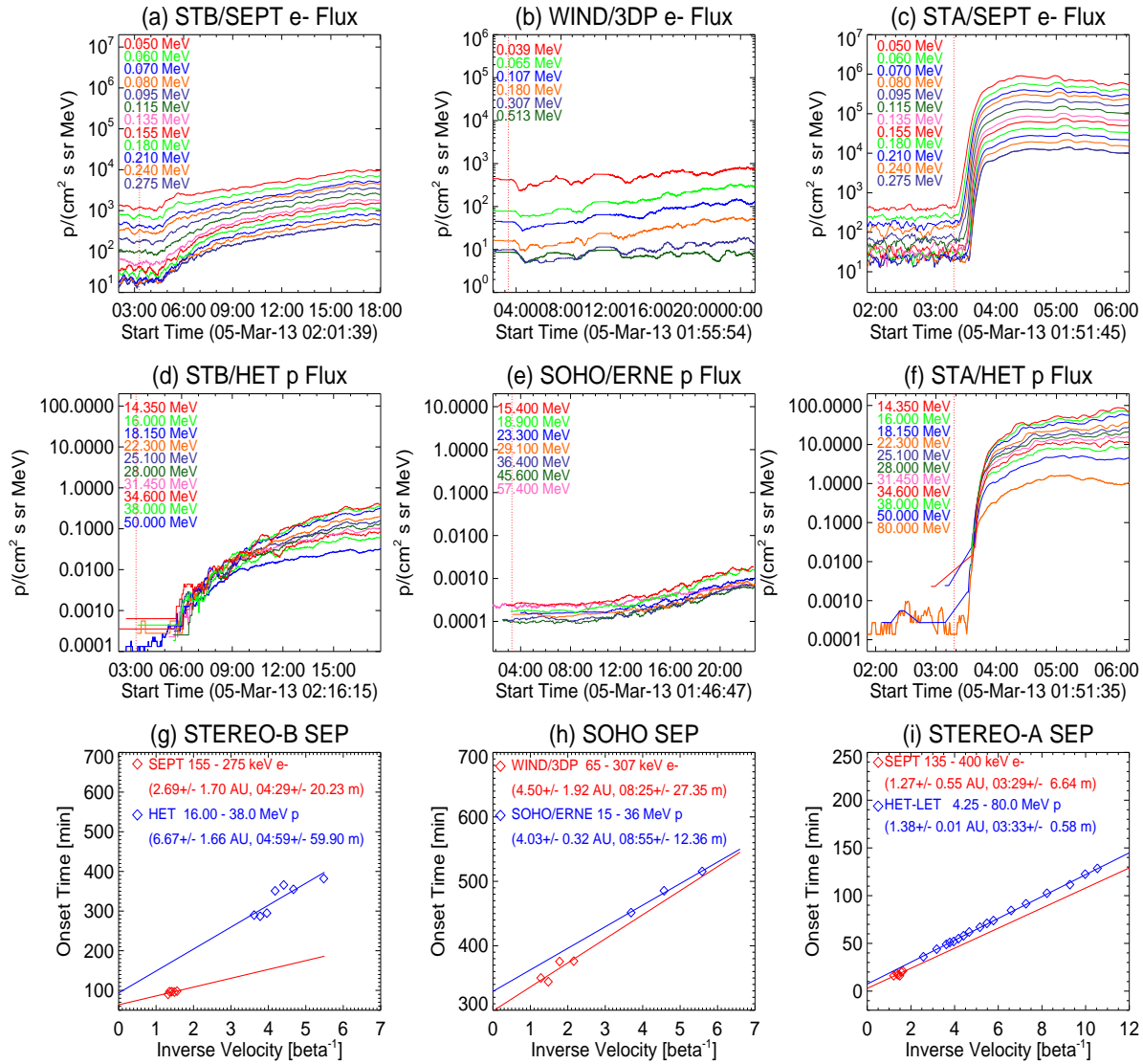


Figure 4. Electron and proton fluxes of the 2013 March 05 SEP event: (a)-(c) electron intensities from STB/SEPT, WIND/3DP and STA/SEPT, (d)-(f) proton intensities from STB/HET, SOHO/ERNE and STA/HET and (g)-(i) the VDA results for the three locations. The red vertical dashed lines in the first and second rows mark the onset time of the associated type III radio burst.

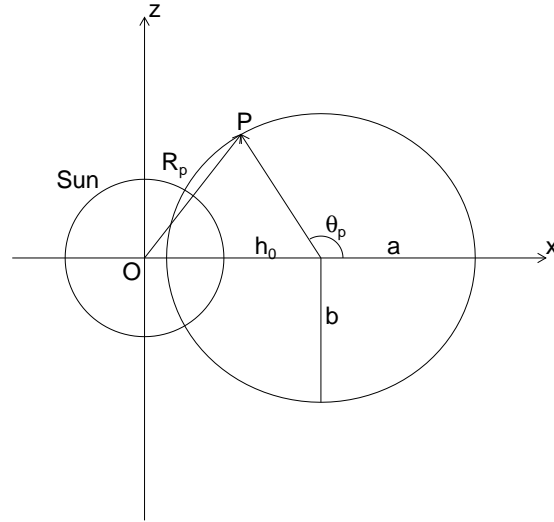


Figure 5. A schematic of the oblate spheroid model drawn on its symmetry plane (x - z plane), where h_0 is the distance of the spheroid center from the solar center O , a and b are semi-major and semi-minor axes of the ellipse, R_p is the heliocentric distance and θ_p is the polar angle from the spheroid center for a given point P on a shock model surface.

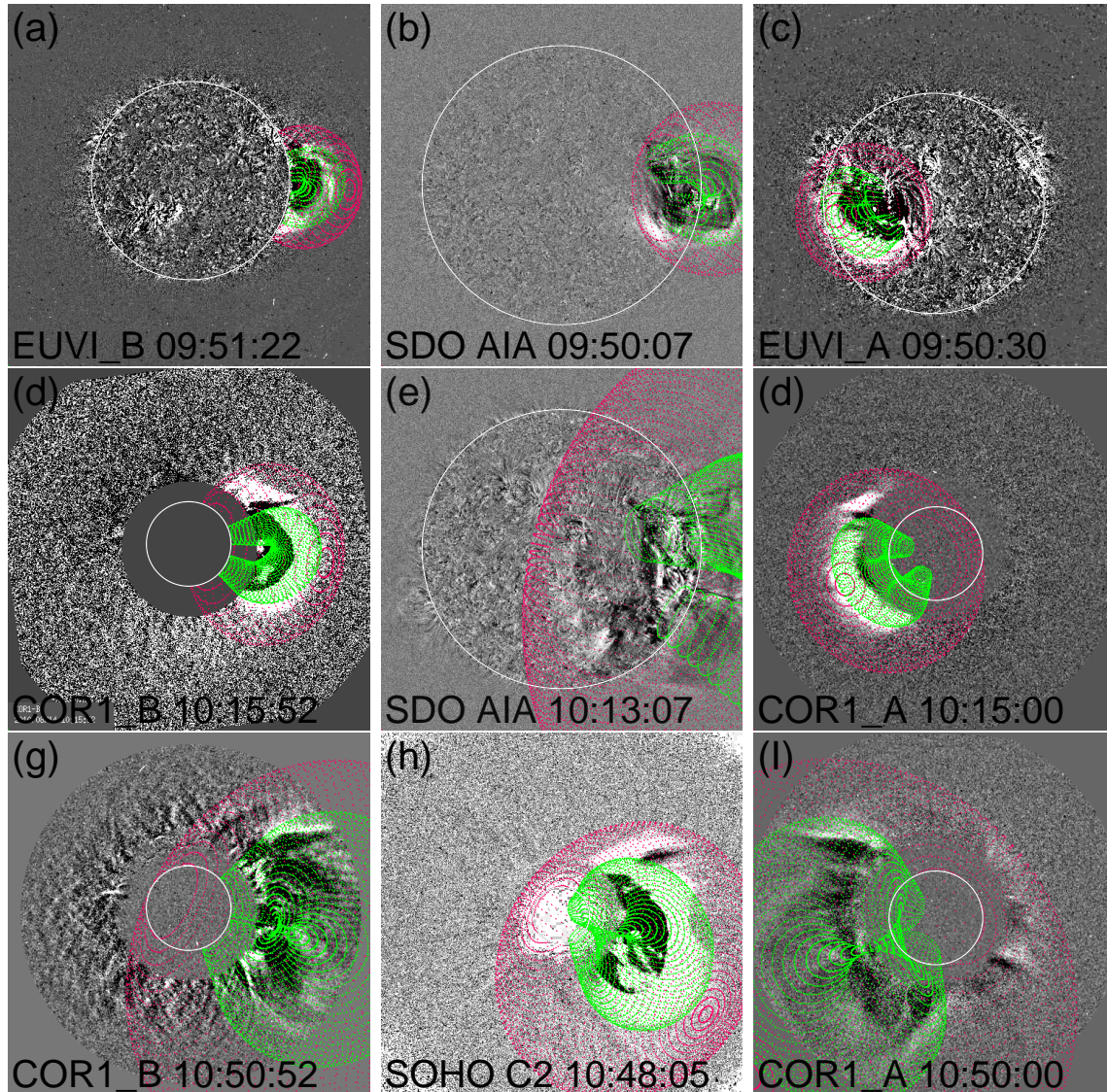


Figure 6. From left to right: views from STB, SOHO, and STA of the CME-shock structure with the oblate spheroid shock model (red wireframe) and the CME flux rope model (green wireframe) superimposed on them at three different times during the 2010 August 14 eruption.

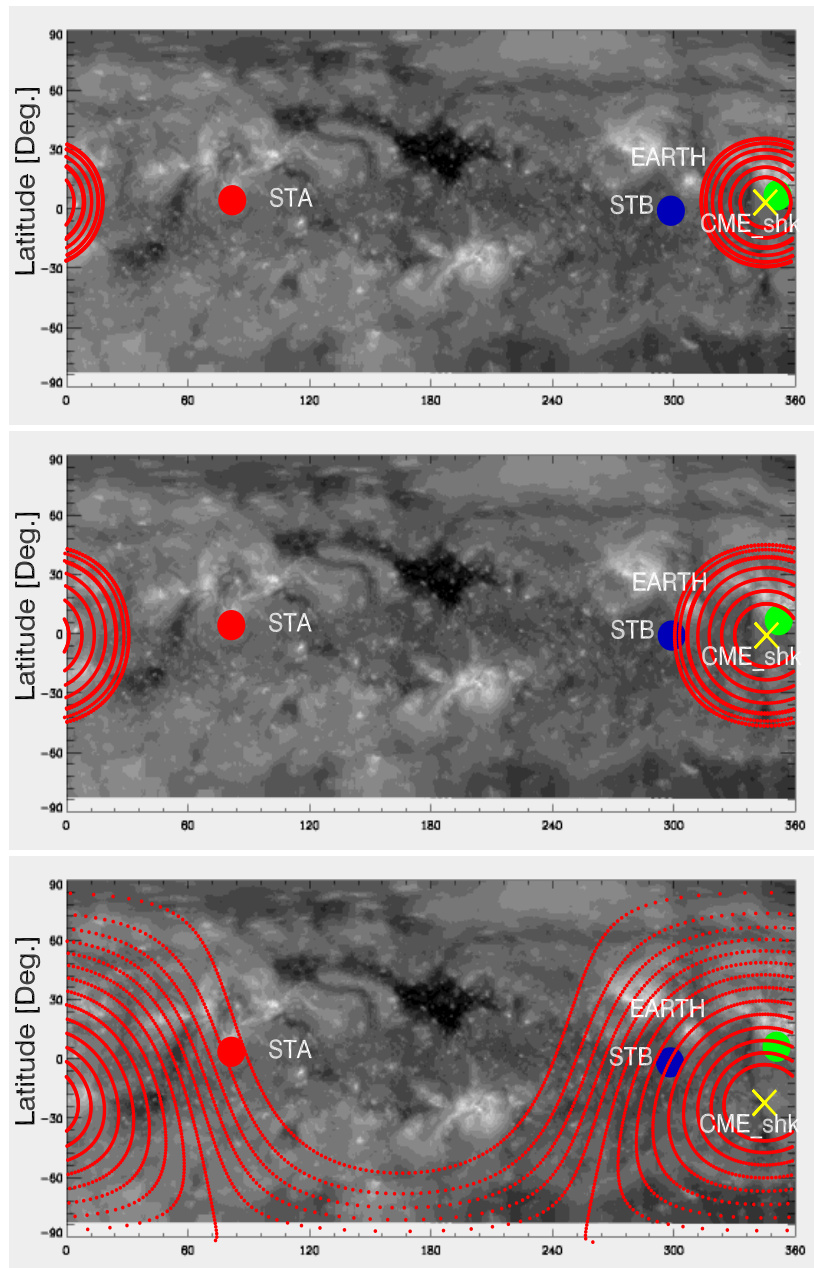


Figure 7. The projection of the fitted shock model on the solar surface plotted as a series of red circular contours superimposed on a Carrington map of 195 \AA EUVI images. The magnetic footpoints of STA, STB and Earth are marked with red, blue, green dots, along with the location of the CME-shock nose (yellow cross) on 2010 August 14. From top to bottom panels the shock propagation shown at times of 09:50 UT, 10:00 UT and 10:40 UT, respectively.

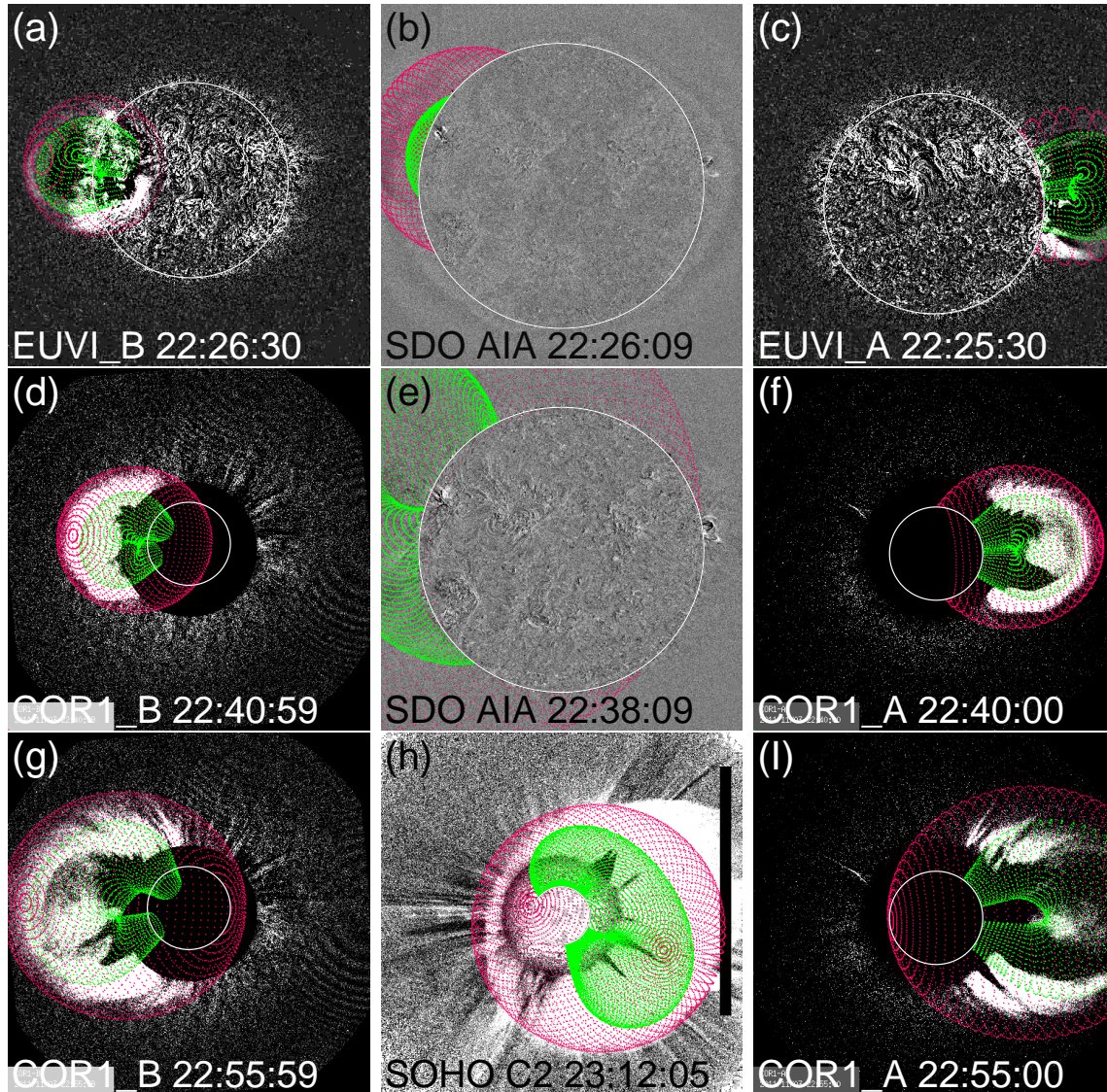


Figure 8. From left to right: views from STB, SOHO, and STA of the CME-shock structure with the oblate spheroid shock model (red wireframe) and the CME flux rope model (green wireframe) superimposed on them at three different times during the 2011 November 03 eruption.

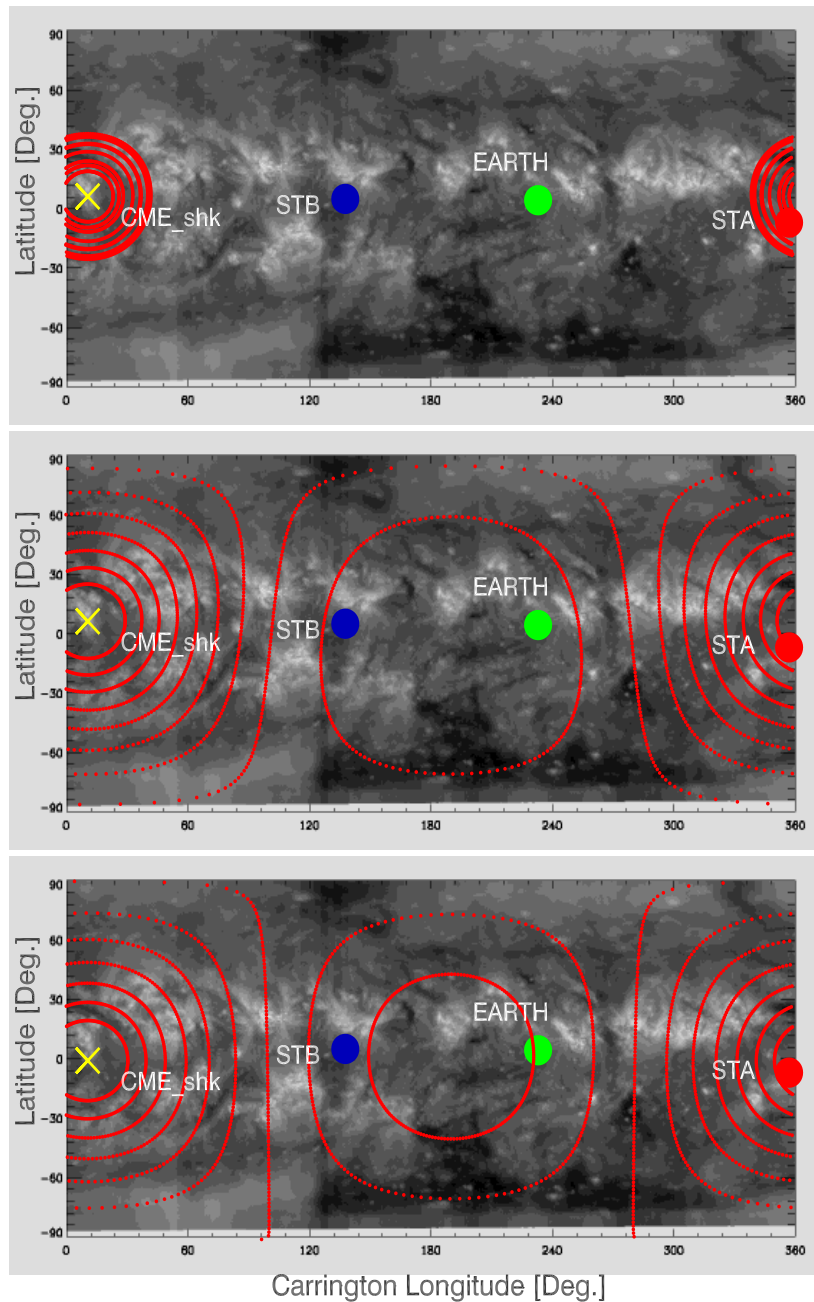


Figure 9. The projection of the fitted shock model on the solar surface plotted as a series of red circular contours superimposed on a Carrington map of 195 \AA EUVI images. The magnetic footpoints of STA, STB and Earth are marked with red, blue, green dots, along with the location of the CME-shock nose (yellow cross) on 2011 November 03. From top to bottom panels the shock propagation shown at times of 22:25 UT, 22:40 UT and 22:55 UT, respectively.

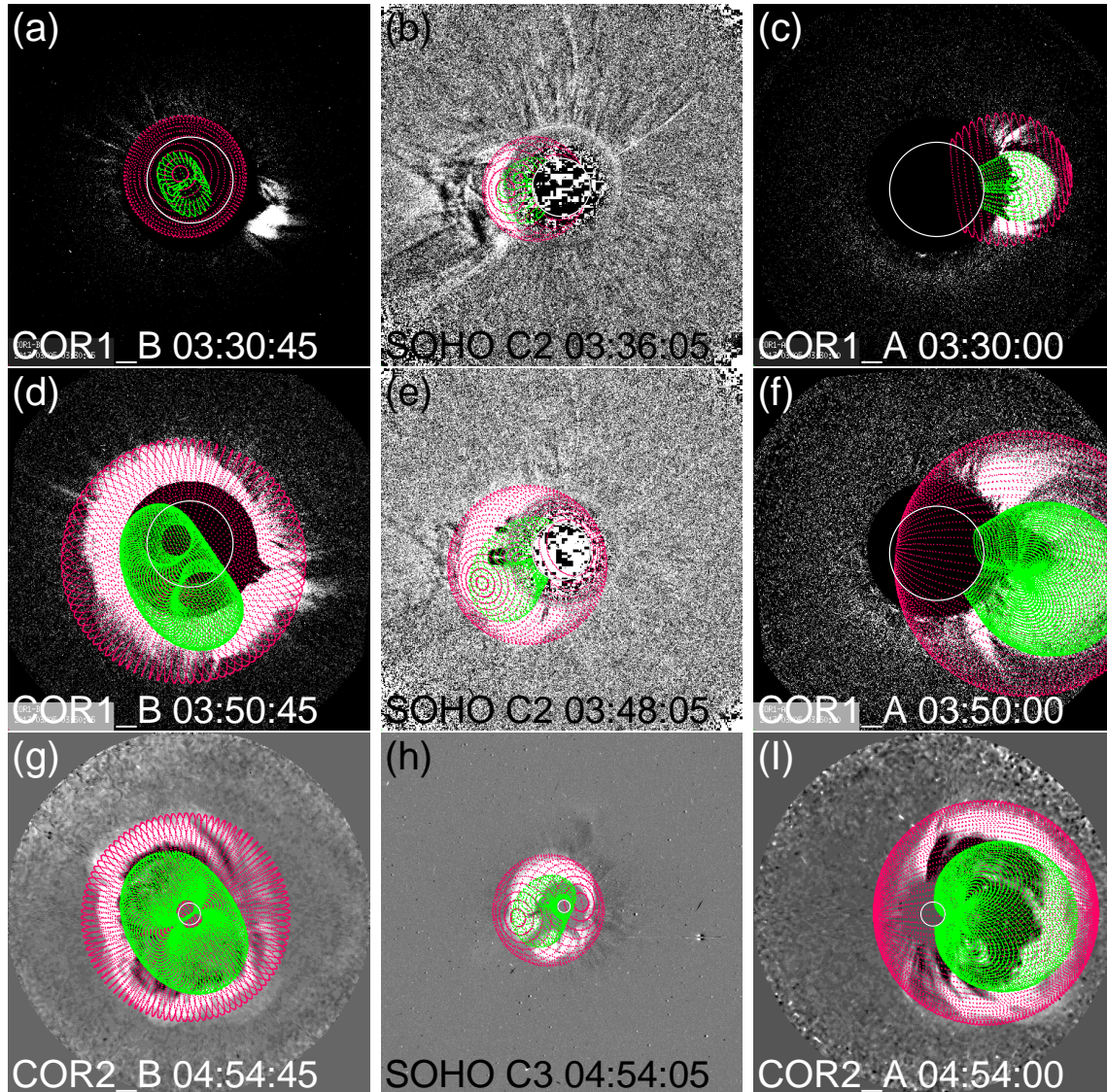


Figure 10. From left to right: views from STB, SOHO, and STA of the CME-shock structure with the oblate spheroid shock model (red wireframe) and the CME flux rope model (green wireframe) superimposed on them at three different times during the 2013 March 05 eruption.

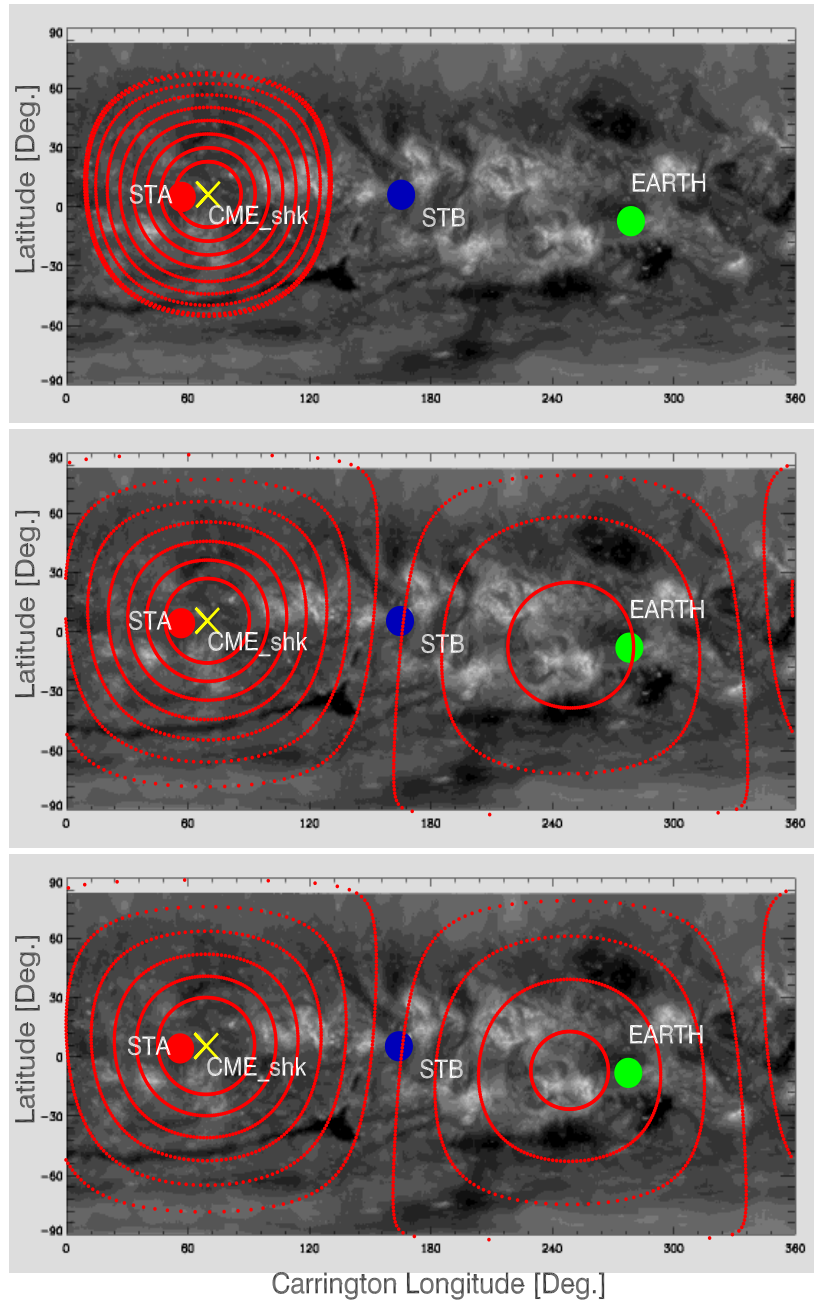


Figure 11. The projection of the fitted shock model on the solar surface plotted as a series of red circular contours superimposed on a Carrington map of 195 \AA EUVI images. The magnetic footpoints of STA, STB and Earth are marked with red, blue, green dots, along with the location of the CME-shock nose (yellow cross) on 2013 March 5. From top to bottom panels the shock the shock propagation shown at times of 03:30 UT, 03:55 UT and 04:54 UT, respectively.

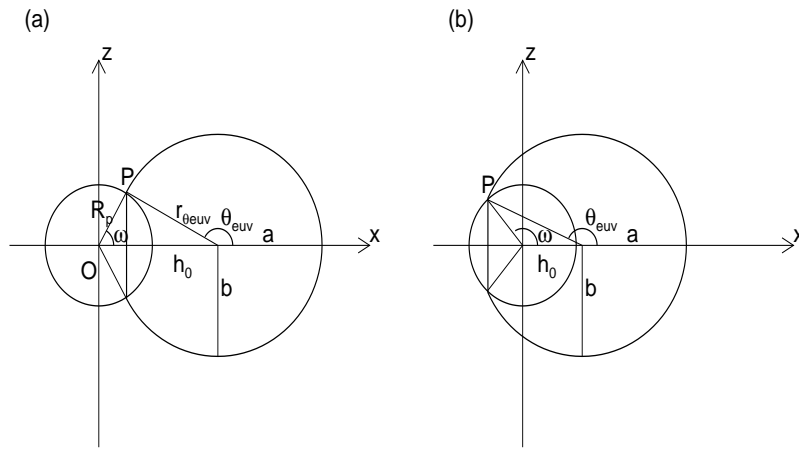


Figure 12. A schematic of the oblate spheroid model drawn on its symmetry plane (x - z plane) for shock half width (a) $\omega < 90^\circ$ and (b) $\omega > 90^\circ$.

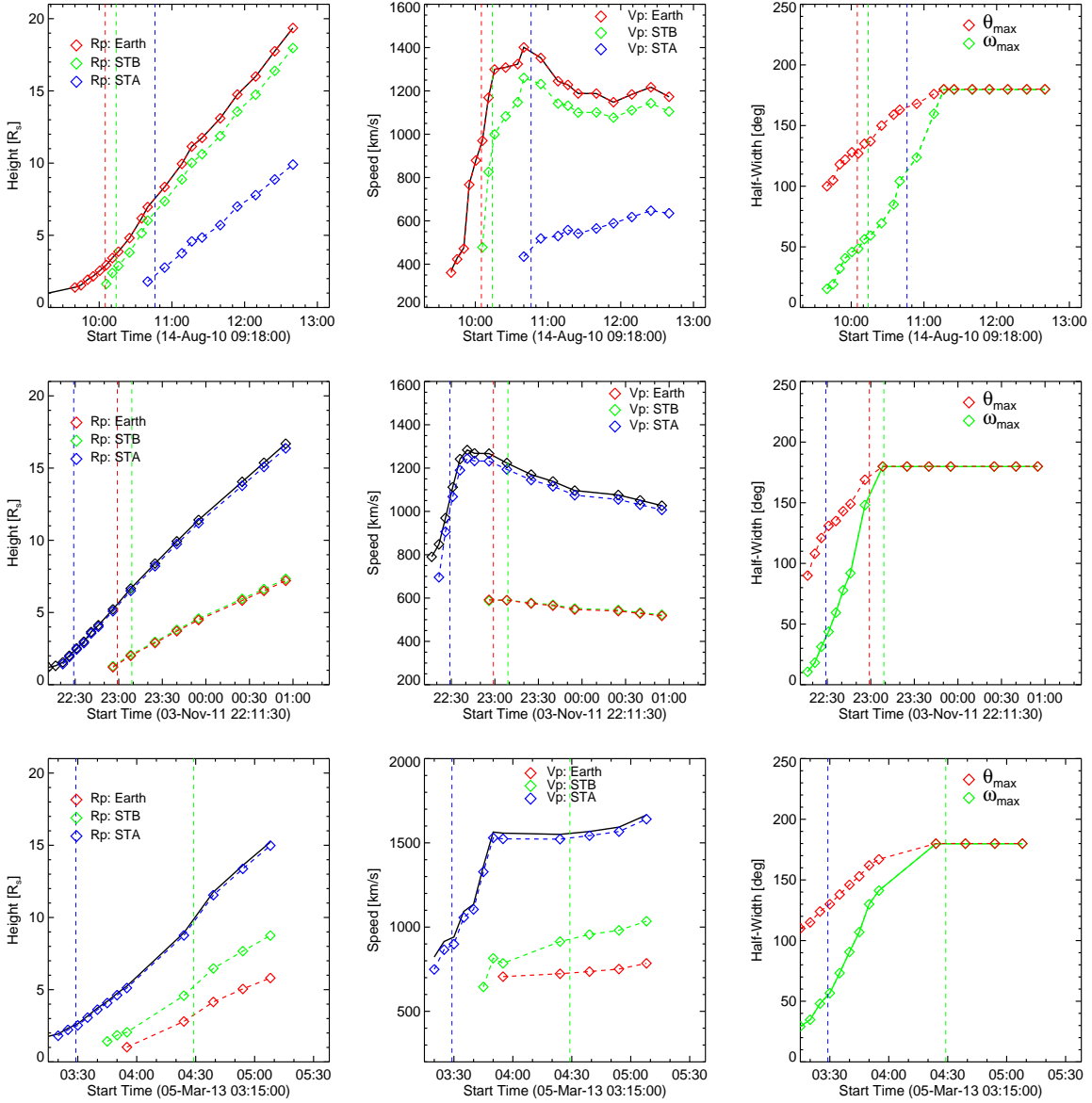


Figure 13. (Left) Heliocentric distance, R_p , (middle) shock speed, $V_p = dR_p/dt$, at cobpoints and (right) shock half width ω and maximum polar angle θ_p as a function of time. Vertical dashed lines mark the SEP electron release times for near-Earth spacecraft (red), STB (green), and STA (blue).

Table 1. Solar Observations for the Three SEP Events

#	Date	Flare		Vcme Vsky/Vspace (km/s)	T-III (UT)	T-II m-II/DH (UT)	CA		
		Onset (UT)	Loc				STB	L1 (°)	STA
1	2010/08/14	09:38	N17W52	1205/1280	09:56	09:52/-:-	48	4	-92
2	2011/11/03	20:16	N09E154	991/1188	22:17	-:/22:35	-130	135	11
3	2013/03/05	03:06	N10E144	1316/1498	03:18	-:/03:30	-94	152	14

Table 2. Spacecraft Locations and Solar Wind Speeds

#	Date	Flare Onset (UT)	SC/Loc		Vsw		
			STB	STA (°)	STB	L1 (km/s)	STA
1	2010/08/14	09:38	E71	W79	332	444	374
2	2011/11/03	20:16	E102	W105	319	348	276
3	2013/03/05	03:06	E140	W131	274	389	349

Table 3. Solar Particle Release Times at the Three Spacecraft

#	Date	Particle	SPR		
			STB	L1 (UT \pm min)	STA
1	2010/08/14	e-	10:14 \pm 3.4	10:05 \pm 1.6	10:46 \pm 30
		p	10:22 \pm 8.4	10:10 \pm 1.8	11:06 \pm 36.4
2	2011/11/03	e-	23:09 \pm 10.9	22:59 \pm 2.4	22:29 \pm 1.6
		p	23:14 \pm 8.6	23:32 \pm 20.9	22:38 \pm 7.4
3	2013/03/05	e-	04:29 \pm 20.2	08:25 \pm 27.4	03:29 \pm 6.6
		p	04:59 \pm 59.9	08:55 \pm 12.4	03:33 \pm 10

Table 4. Time Delays of SPR Times and Magnetic Connection Times at the Three Spacecraft

#	Date	Particle	MCT			Time Delay of SPR		
			STB	L1 (UT)	STA	STB	L1 (min)	STA
1	2010/08/14	e-	10:01	09:52	10:37	13	13	9
		p				21	18	29
2	2011/11/03	e-	22:52	22:55	22:17	17	4	12
		p				22	37	21
3	2013/03/05	e-	03:42	03:57	03:18	47	268	11
		p				77	298	15

Table 5. Height and Speed of the Shock at cobpoints at SEP Release Times

#	SEP	R_p			V_p			θ_p			ω_{max}		
		STB/L1/STA	STB/L1/STA	STB/L1/STA	STB/L1/STA	STB/L1/STA	STB/L1/STA	STB/L1/STA	STB/L1/STA	STB/L1/STA	STB/L1/STA	STB/L1/STA	
		$(R_s \pm \text{unt})$			(km/s)			(deg)			(deg)		
Evt1	e-	2.78±0.28	2.94±0.13	2.22±1.09	964	970	471	97	10	149	59	49	113
	p	3.53±0.77	3.43±0.18	3.62±1.62	1057	1169	528	91	10	142	66	56	155
Evt2	e-	2.13±0.47	1.45±0.11	2.34±0.14	590	591	1036	158	164	31	180	158	41
	p	2.40±0.37	3.33±0.88	3.28±0.71	586	569	1222	157	158	24	180	180	70
Evt3	e-	5.22±1.58	—:—	2.47±0.51	928	—	892	127	—	33	180	—	55
	p	8.06±5.04	—:—	2.85±0.91	1000	—	994	124	—	31	180	—	67